Chemical Geology 692 (2025) 122961

Contents lists available at ScienceDirect

Chemical Geology

journal homepage: www.elsevier.com/locate/chemgeo

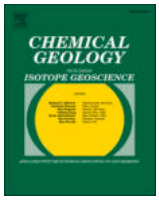

Research Paper

Fe isotope systematics and their role in constraining front- and rear-arc processes in Iran Cenozoic magmatism: Beyond compositional and radiogenic isotopes evidence

Shahrouz Babazadeh [a,*], Yajun An [b,c], M. Santosh [d,e], Tanya Furman [f], Davood Raeisi [g], Behnam Gholipour [h], Massimo D'Antonio [i,*]

[a] Natural Science Research Institute, Chungnam National University, Daejeon 34134, Republic of Korea
[b] International Centre for Planetary Science, College of Geosciences, Chengdu University of Technology, Chengdu 610059, China
[c] State Key Laboratory of Isotope Geochemistry, Guangzhou Institute of Geochemistry, Chinese Academy of Sciences, Guangzhou 510640, PR China
[d] School of Earth Sciences and Resources, China University of Geosciences Beijing, Beijing 100083, PR China
[e] Department of Earth Science, University of Adelaide, Adelaide, SA 5005, Australia
[f] Department of Geosciences, Pennsylvania State University, University Park, PA 16802, USA
[g] School of Geology, College of Science, University of Tehran, Tehran, Iran
[h] Department of Geology, Tarbiat Modares University, Tehran 14115-175, Iran
[i] Dipartimento di Scienze della Terra, dell'Ambiente e delle Risorse - DiSTAR, University Federico II, I-80126 Naples, Italy

ARTICLE INFO

Editor: S Aulbach

Keywords:
Cenozoic frontal- and rear-arc Eocene-
–Oligocene magmatism
Iran
Fe isotope composition
Redox evolution
Fractional crystallization

ABSTRACT

The Cenozoic arc of Iran preserves archetypal exposures of the continental arc developed during the north-eastward subduction of the Neo-Tethys oceanic slab and records the history of flare-up magmatism within the Zagros Orogen. Here we present a new dataset of high-precision Fe–Sr–Nd isotopic compositions of Eocene-–Oligocene frontal- and rear-arc (*i.e.*, pre-collisional) magmatic products associated with subduction of the Neo-Tethys Ocean beneath Iran to provide new constraints on the fractionation of Fe isotopes and cycling of Fe within these tectonic settings. The δ^{56}Fe values range from +0.07 ‰ to +0.15 ‰, falling within the range of arc-related rocks worldwide. The rear arc samples display higher δ^{56}Fe (+0.135 ± 0.010 (2σ)) than samples from the coeval frontal arc (+0.090 ± 0.006 (2σ)). The low $Fe^{3+}/\Sigma Fe$ values of all investigated samples in the range from 0.26 to 0.36 and the lack of negative correlation between δ^{56}Fe and $Fe^{3+}/\Sigma Fe$ argue against incorporation of any significant sulfate- and/or carbonate-bearing fluids. Based on geochemical and isotopic data, we postulate that the high-flux magmatic events (*i.e.,* flare-ups) are related to partial melting of a garnet-free lherzolite mantle source and limited crustal assimilation. Our results also demonstrate that the Fe isotope fractionation in the Zagros orogen is primarily governed by fractional crystallization of Fe^{2+}-rich phases (*e.g.*, olivine, clinopyroxene), particularly in rear-arc domains where deeper crystallization promotes heavier δ^{56}Fe signatures. Although changes in oxidation state can affect Fe isotope fractionation when iron is added or lost from the system, the relatively narrow range in $Fe^{3+}/\Sigma Fe$ ratios and the absence of a systematic covariation with δ^{56}Fe suggest that redox-driven effects were likely secondary with respect to crystal–melt partitioning in this setting. This stands in marked contrast to global arc systems, particularly oceanic arcs, where slab-derived oxidizing fluids typically dominate over magmatic differentiation, underscoring the Zagros as a case where source composition and fractional crystallization outweigh subduction-related redox processes.

1. Introduction

Arc settings along convergent margins play a critical role in mediating the exchange of elements between the Earth's deep mantle and crust, influencing the protracted cycling of redox-sensitive elements such as Fe, C, and S, which are mobilized through slab-derived fluids and melts. Understanding Fe isotope variations in such settings is essential to unravel the mechanisms controlling mantle wedge oxidation state (*i.e.*, the balance between oxidation and reduction) and subsequent magma genesis (*e.g.,* Debret et al., 2020). The redox-sensitive elements are

* Corresponding authors.
E-mail addresses: shahrouz.babazadeh@gmail.com (S. Babazadeh), masdanto@unina.it (M. D'Antonio).

https://doi.org/10.1016/j.chemgeo.2025.122961
Received 8 January 2025; Received in revised form 9 July 2025; Accepted 11 July 2025
Available online 13 July 2025

pivotal because their redox state affects key processes, including the formation of minerals, nutrient availability, and even atmospheric and oceanic chemistry. By examining the cycle of such elements within arc settings, we gain insights into the interconnected processes that govern Earth's long-term geochemical evolution.

Partial melting of the mantle and differentiation of the resulting magmas lead to redistribution of incompatible trace elements, although the elemental abundances alone are insufficient indicators to evaluate the variability of source mineralogy and/or lithology (*e.g.,* Hofmann, 1997). Fe isotopes provide alternative proxies to track source contributions and subsequent processes in arc settings including the role of slab-derived components (*e.g.,* fluids and melts), oxygen fugacity, and magma differentiation (*e.g.,* Dauphas et al., 2014). Previous studies have shown that enriched mid-ocean ridge basalts (*E*-MORBs) have a restricted range of δ^{56}Fe values ($\delta^{56}Fe = +0.11 \pm 0.04$ ‰; Teng et al., 2013; Chen et al., 2019) that contrast with depleted MORBs which show lower δ^{56}Fe values (*e.g.,* +0.05 ‰ to +0.10 ‰; Williams et al., 2018; McCoy-West et al., 2019). Ophiolitic and abyssal peridotites are characterized by distinct δ^{56}Fe values of -0.030 ± 0.143 ‰ and $+ 0.010 \pm 0.007$ ‰, respectively (*e.g.,* Nebel et al., 2015). Island arc magmas have variable δ^{56}Fe values (from −0.15 to +0.19 ‰; Dauphas et al., 2009; Nebel et al., 2015; Foden et al., 2018), whereas OIBs show a more restricted range, +0.09 to +0.18 ‰. The low δ^{56}Fe values in the OIBs are attributed to contributions from serpentinite-derived fluids (*e.g.,* Huang et al., 2020) or depletion of components with low δ^{56}Fe values in the mantle sources through persistent melt removal under high-fO_2 conditions (*e.g.,* Foden et al., 2018). Back-arc basin basalts display substantial variability in δ^{56}Fe values, ranging from −0.01 to +0.19 ‰ (*e.g.,* Teng et al., 2013) whereas the continental arc magmas show heavier δ^{56}Fe values (+0.08 ‰ to +0.18 ‰; Poitrasson and Freydier, 2005; Telus et al., 2012; Chen et al., 2021). Notably, global arc magmas display widely variable, still on average lighter Fe isotopic compositions (especially those from oceanic settings: $\delta^{56}Fe \approx +0.03$ to +0.10 ‰; Foden et al., 2018; Nebel et al., 2019; Chen et al., 2021) compared to MORB, which is unexpected if mantle wedges were similar to merely oxidized depleted MORB mantle (DMM). This paradox points to a complex interplay among slab-derived fluids, mantle melting processes, and likely mineral fractionation. Supplementary Fig. S1 provides a compilation of δ^{56}Fe ranges for different rock types from the abovementioned literature. The Fe isotope variations in arc settings are attributed to various processes, including (*i*) mantle redox conditions and complexation of iron with carbonate and/or sulfate ligands (Fe(II)-CO_3 or Fe(II)-SO_4; *e.g.,* Debret et al., 2020), (*ii*) transferring Fe^{3+} and other fluid-immobile and trivalent elements directly *via* supercritical fluids (*e.g.,* Kelley and Cottrell, 2009), (*iii*) retention and/or fractionation of Fe^{2+}-rich minerals (*e.g.,* garnet and amphibole; $Fe^{3+}/\Sigma Fe \leq 0.1$; Tang et al., 2019), and (*iv*) open–system mantle–crust mixing and/or intra-crustal differentiation. Therefore, δ^{56}Fe is a sensitive tracer of magmatic petrogenesis. Accordingly, heavier δ^{56}Fe values typically indicate more oxidized or differentiated magmas, retention and/or fractionation of Fe^{2+}-rich minerals, open–system mantle–crust mixing and/or intra-crustal differentiation, while lighter values suggest less oxidized or more primitive magmas.

To date, no previous studies have applied the Fe isotopes systematics to Cenozoic magmatism of Neo-Tethys regions such as Iran, Turkey, and Armenia. Magmatism associated with Neo-Tethys is characterized by significant tectonic complexity and plays a crucial role in subduction zone dynamics, making it an ideal case for understanding Fe isotopes behavior in arc magmatism. While Fe isotopes have been extensively used to study igneous processes, this study is unique in its application to both frontal- and rear-arc settings—a comparison that has not been systematically explored either in this region or globally. The frontal- and rear-arc regions are influenced by different geodynamic processes that shape their magmatic characteristics. In the frontal arc, magmatism is primarily driven by the interaction between the subducting slab and the overlying mantle wedge, resulting in volcanic products with radiogenic isotope signatures reflecting a significant role for mantle-derived melts. Fe isotopes in such geodynamic setting are sensitive to the extent of mantle melting, slab-derived fluid input, and redox conditions in the mantle wedge (*e.g.,* Dauphas et al., 2017; Williams et al., 2018; Wang et al., 2020). In contrast, the rear arc is typically influenced by processes such as magmatic differentiation, with relatively lower degrees of mantle involvement. As a result, Fe isotopic compositions in rear arc settings provide valuable insights into the role of magmatic differentiation (*e.g.,* Heimann et al., 2008; Teng et al., 2013; Sossi et al., 2016).

The Zagros orogeny, an epitome of an Andean-type continental arc developed during north-eastward subduction of the Neo-Tethys oceanic slab beneath Iran plate, preserves the record of Cenozoic flare-ups. By investigating the frontal- and rear-arc settings of the Zagros orogeny within a unified tectonic framework, we explore how different magmatic processes influence Fe isotopic fractionation. The results of this case study provide new perspectives on the use of Fe isotopes as tracers in subduction zones, thereby advancing our understanding of arc magmatism not only in the Neo-Tethys but also in other subduction-related environments worldwide. The geochemical and isotopic data presented here provide insights into the mechanisms that drove magmas toward heavier ^{56}Fe values including the nature and role of (*i*) type of the mantle source(s); (*ii*) metasomatic melts and exsolved fluids, (*iii*) open–system mantle–crust mixing, and (*iv*) mineral–melt fractionation.

2. Geological background

The Zagros orogen represents a prominent segment of the Arabia–Eurasia collision zone, which developed from the Late Cretaceous (~110 Ma) to Pleistocene as a result of the subduction of Neo-Tethyan oceanic crust beneath the Iranian Plateau (*e.g.,* Berberian and Berberian, 1981). Subduction was accompanied by the development of a linear NW–SE trending magmatic front in central Iran known as the Urumieh–Dokhtar magmatic arc (UDMA), and an E–W arcuate rear arc in NE Iran (Fig. 1). Frontal arc magmatism can be divided into two main stages: ~80–71 Ma (Late Cretaceous) and ~ 54–5.5 Ma (Eocene to Miocene), culminating with a magmatic flare-up in the Middle Eocene (*e.g.,* Berberian and Berberian, 1981). Rear arc magmatism in northeast Iran was initiated in the latest Cretaceous (104–76 Ma), continued with a prolonged Eocene flare-up, and closed with significant mitigation of magmatic activities through the Neogene–Pleistocene. Subduction continued with a "*soft*" collision at ~32 Ma (Early Oligocene; McQuarrie and van Hinsbergen, 2013; Pirouz et al., 2017), followed by a "*hard*" collision at ~20–15 Ma (Early-to Middle Miocene; Moghadam et al., 2022a). Alternatively, evidence from the geochemical, Sr– Nd isotopic and U—Pb radiometric data suggests the "hard" collision might have initiated ~15–11 Ma ago (*e.g.,* Chiu et al., 2013; Pang et al., 2013; Babazadeh et al., 2023). During the Eocene (55 to 23 Ma), thinning of arc crust occurred within an extensional tectonic regime, although not at the same rate throughout Iran (*e.g.,* Verdel et al., 2011). A significant tectonic and magmatic transition from subduction-type to collisional-type magmatism occurred during the Miocene–Quaternary, marking a shift from an extensional to a contractional tectonic regime (*e.g.,* Moghadam et al., 2022a). This transition is characterized by a decline in typical arc-related magmatism and the appearance of magmatic signatures indicative of crustal thickening and lithospheric compression. The evolving magmatic compositions reflect continued mantle contributions that were modified by tectonic processes associated with the final stages of Arabian-Eurasian plate collision. This shift underscores the role of continental collision in altering magmatic activity and composition, contributing valuable insights into crustal evolution and modification within the Zagros orogen.

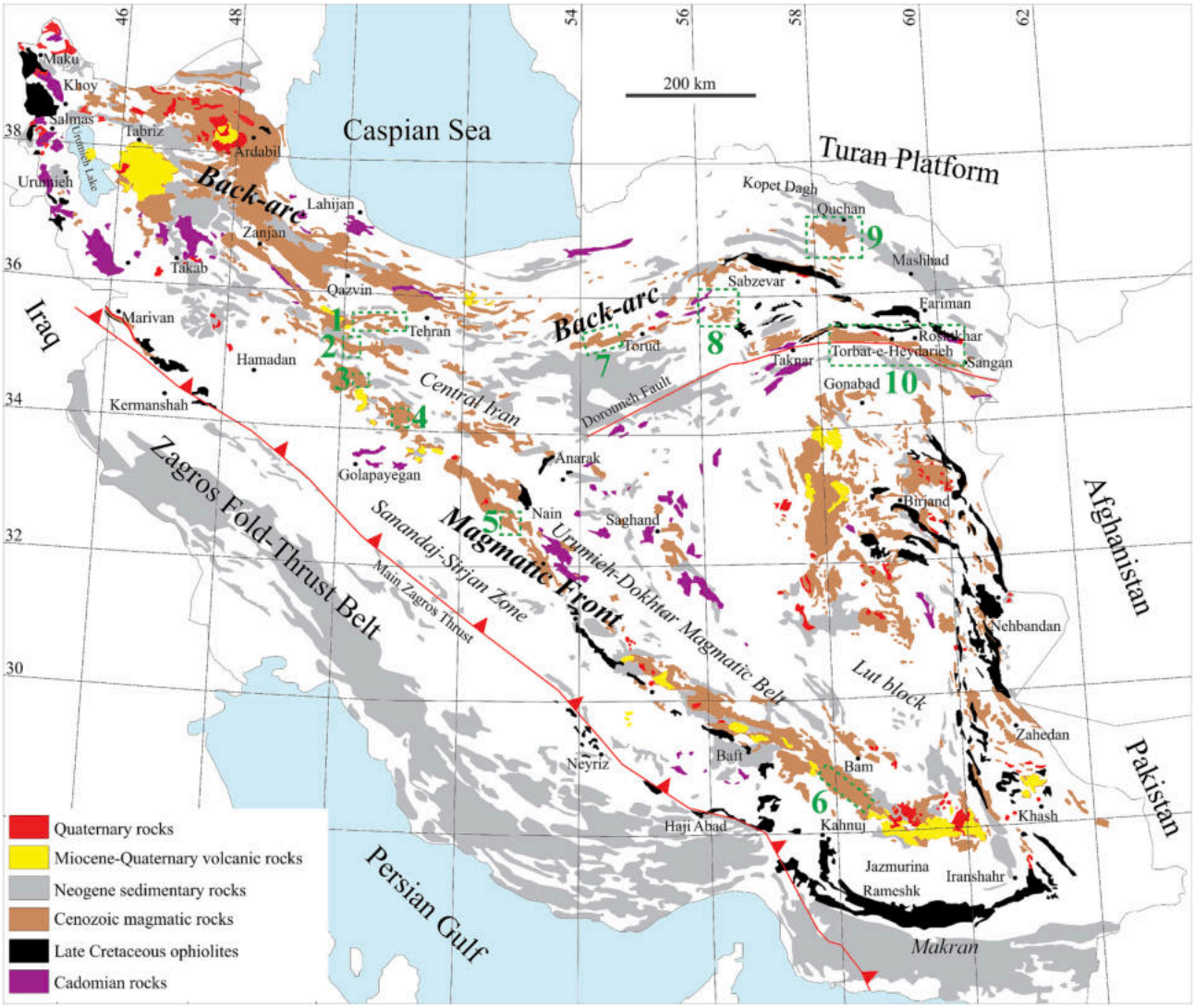

Fig. 1. Geological map of Iran showing distribution of Paleozoic to Cenozoic lavas in Iran. Regions 1 to 6 are associated with the frontal arc, while regions 7 to 10 are linked to the rear arc. The regions are indicated as follows: 1 = Eshtehard; 2 = Saveh; 3 = Qom; 4 = Natanz; 5 = Nodoushan; 6 = SE UDMA; 7 = Moalleman; 8 = Sabzevar; 9 = Quchan; 10 = Roshtkhar–Torbat-e-Heydarieh.

3. Sampling and analytical methods

3.1. Sample selection and preparation

The Eocene to Oligocene magmatic suites studied here consist of 30 predominantly mafic to subordinate intermediate volcanic–plutonic rocks, representing a differentiation series generated before the main Iran–Arabia collision and crustal thickening (*i.e.*, < 20–15 Ma). Weathered and hydrothermally altered units were excluded based on detailed petrographic examination (identifying primary mineral preservation and absence of secondary alteration features) and only samples with loss on ignition (L.O.I.) lower than 3 wt% were selected for analysis (Appendix Table S1).

3.2. Whole rock geochemistry

For whole-rock analysis, the selected samples were crushed into <0.5-cm-sized fragments in a tungsten carbide mortar and then cleaned ultrasonically with Milli-Q water. Fresh fragments that were free of visible surface alteration were handpicked (400 g) and powdered with an agate ball mill. Whole-rock major and trace element concentrations were determined by inductively coupled plasma optical emission spectrometry (ICP–OES) and ICP mass spectrometry (ICP–MS), respectively, at Act Labs, Ontario, Canada. Elements data were processed with weighted regression lines based on analysis of international reference materials, including *e.g.*, W-2a, DNC-1, and BIR-1. The analytical precision of major oxides is estimated as ±5 %. Trace element concentrations have a precision of ±10 %, based on replicate analyses of international standards (SDC-1, SBC-1, and DNC-1a; see Appendix Table S2).

3.3. Sr − Nd isotopes

Sr- and Nd-isotope analyses were carried out at the Chinese Academy of Geological Sciences, Beijing (CAGS), and at the Wuhan Sample Solution Analytical Technology Co., Ltd., China (WSSTC). Fresh rock chips were carefully selected to avoid weathered or altered portions. These samples were cleaned, crushed, and powdered to a fine grain size (<200 mesh) using an agate mill to prevent contamination. Approximately 50–100 mg of the powdered sample was weighed and transferred to a clean Teflon beaker for chemical dissolution. The powdered samples were digested using a mixture of concentrated HF and HNO_3 in a tightly sealed Teflon digestion bomb at 120–180 °C for 48 h to ensure complete dissolution of silicate minerals. Following evaporation to dryness, the

residue was dissolved in 6 M HCl and evaporated again to remove fluorides. The final residue was re-dissolved in 3 M HNO_3 for ion exchange chromatography. Strontium was separated using Sr-Spec® resin. The matrix elements were removed through sequential washing steps with 3 M HNO_3, and Sr was eluted using 0.05 M HNO_3. Rare earth elements (REEs) were first separated from the sample solution using cation exchange resin (AG50W-X8). Neodymium was further purified from the REE fraction using HDEHP (di(2-ethylhexyl) orthophosphoric acid)-coated resin. The resulting Nd fraction was collected in 0.25 M HCl.

For analyses made at CAGS, the purified Sr and Nd fractions were loaded onto single Re filaments (for Sr) and double Re filaments (for Nd) for thermal ionization mass spectrometry (TIMS). $^{87}Sr/^{86}Sr$ ratios were measured and corrected for instrumental mass fractionation using $^{86}Sr/^{88}Sr = 0.1194$. The accuracy of the analysis was ensured using the international standard NIST–SRM 987, which yielded $^{87}Sr/^{86}Sr = 0.710250 \pm 0.000010$ (2σ). $^{143}Nd/^{144}Nd$ ratios were corrected for instrumental mass fractionation using $^{146}Nd/^{144}Nd = 0.7219$ as the normalization factor. The international standard JNdi-1 was analyzed, yielding $^{143}Nd/^{144}Nd = 0.512115 \pm 0.000010$ (2σ). Procedural blanks were consistently below the detection limit, and replicate analyses of samples and standards demonstrated high precision, with typical uncertainties of ±0.00002 for $^{87}Sr/^{86}Sr$ and $^{143}Nd/^{144}Nd$. Duplicate analyses of selected samples were within analytical error, confirming data reliability.

At WSSTC, the isotopic analyses were performed on purified fractions of Sr and Nd using TIMS. The Sr and Nd fractions were loaded onto single and double rhenium (Re) filaments, respectively, to facilitate ionization. Isotope ratios ($^{87}Sr/^{86}Sr$ and $^{143}Nd/^{144}Nd$) were measured, and instrumental mass fractionation was corrected using $^{86}Sr/^{88}Sr = 0.1194$ and $^{146}Nd/^{144}Nd = 0.7219$ as normalization factors, respectively. The measured values for the NIST-SRM 987 Sr standard ($^{87}Sr/^{86}Sr = 0.710244 \pm 0.000008$, 2σ, $n = 7$) and GSB 04–3258-2015 Nd standard ($^{143}Nd/^{144}Nd = 0.512441 \pm 0.000007$, 2σ, n = 7) were consistent with their published values ($^{87}Sr/^{86}Sr = 0.710248 \pm 0.000012$, Zhang and Hu, 2020; $^{143}Nd/^{144}Nd = 0.512438 \pm 0.000005$, Li et al., 2017). Procedural blanks were below 0.04 ppb for Rb, 0.3 ppb for Sr, 0.02 ppb for Sm, and 0.05 ppb for Nd, ensuring minimal contamination. USGS reference standards BCR-2 (basalt) and RGM-2 (rhyolite) were analyzed alongside samples. The measured $^{87}Sr/^{86}Sr$ and $^{143}Nd/^{144}Nd$ ratios for these standards closely matched the recommended values ($^{87}Sr/^{86}Sr$: 0.70492 ± 0.00055 for BCR-2; $^{143}Nd/^{144}Nd$: 0.512638 ± 0.000018 for BCR-2; $^{87}Sr/^{86}Sr$: 0.71336 ± 0.00014 for RGM-2; $^{143}Nd/^{144}Nd$: 0.512487 ± 0.000014 for RGM-2). All data are listed in the Appendix Table S1.

3.4. Fe isotopes

The whole rock powders of samples were prepared for Fe isotope analyses. About 1 mg of a sample separate was digested in a 7 ml Savillex Teflon beaker with a 3:1 mixture of double-distilled, concentrated HCl and HNO_3 on a hotplate at ~120 °C for 24 h. After complete digestion, samples were prepared in 6 M HCl for chromatographic purification using Bio-Rad 200–400 mesh AG1-X8 anion resin. The purification procedures followed the description in Huang et al. (2011). Matrix elements were removed by 6 M HCl and Fe was collected in 0.4 M HCl, 8 M HCl, and H_2O. The recovery of Fe was >99.5 %. The procedural blanks were less than 6 ng, which is negligible relative to the amount of Fe loaded on the column (~75 μg). The purified sample solutions were analyzed for Fe isotopes using the Neptune-Plus MC-ICP-MS and analyzed with the sample-standard bracketing (SSB) method at the University of Science and Technology of China (USTC), following the procedure described in previous studies (Huang et al., 2011; An et al., 2014). Total procedural blanks for Fe were less than 10 ng, which is insignificant relative to the amount of Fe put through chemical purification (≥ 20 μg). The delta notation values for Fe isotope ratios normalized to the IRMM-14 standard are calculated according to Beard and Johnson (2004) and reported in the Appendix Table S1. Repeated analyses of whole-rock powders show excellent consistency of Fe isotope data. In order to assess the accuracy of our measurements, the USGS whole-rock standards BCR-2 and BHVO-2 were also analyzed, and $\delta^{56}Fe = 0.11 \pm 0.05$ ‰ (2 SD; $n = 9$). The external reproducibility at the USTC is better than ±0.05 ‰ (2SD) based on long-term analyses of two in-house standards UIFe (0.685 ± 0.048 ‰; 2SD; $n = 663$) and GSB (0.719 ± 0.048 ‰; 2SD; $n = 391$) over two years.

To quantify $Fe^{3+}/\Sigma Fe$, the FeO was determined by redox titration using $K_2Cr_2O_7$ solution (Yin and Li, 2011). Sample powders were decomposed with hot (close to boiling) concentrated HF and 1:1 H_2SO_4 for 10 min. The sample solutions were then complexed and buffered by newly boiled, cold boric acid. Ferrous Fe was then titrated by potassium dichromate with two sodium diphenylamine sulfonate as the indicator. Fe_2O_3 and $Fe^{3+}/\Sigma Fe$ were then calculated accordingly, the latter reported with an accuracy of ±10 %. See Appendix Table S1 for data.

4. Results

4.1. Summary of geochemical characteristics

The main geochemical and Fe-isotopic features of the investigated Zagros arc rocks are highlighted in diagrams using a simple distinction between frontal arc and rear arc (Figs. 2 through 8). The same diagrams showing data using a distinct symbol for each investigated igneous complex are provided as Supplementary Figs. S2, S4 and S6 through S11. The data show a narrow compositional spectrum, *e.g.,* SiO_2 49.77–56.28 wt%, Fe_2O_3 6.17–8.93, and MgO 4.29–6.80 wt% for frontal arc samples, and SiO_2 51.43–56.64 wt%, Fe_2O_3 6.31–8.22, and MgO 3.04–5.28 wt% for rear arc samples. Indeed, samples vary from basalt to basaltic andesite and straddle the line between calc-alkaline and shoshonitic affinities (Fig. 2a and b; Supplementary Fig. S2). The data exhibit generally homogenous trends, such as an enrichment in large ion lithophile elements (LILE) and light rare earth elements (LREE), alongside a depletion in high-field strength elements (HFSE) and heavy rare earth elements (HREE; chondrite-normalized patterns are shown in Supplementary Fig. S3). These geochemical signatures are typical of an arc environment (*e.g.,* Pearce and Peate, 1995). Moderate $^{87}Sr/^{86}Sr$ ratios (0.7047–0.7062) and Sr (324–748 ppm) and Y abundances (17–26 ppm) corresponding to Sr/Y values of 13–37 are distinct from those of typical adakitic rocks that display low $^{87}Sr/^{86}Sr < 0.7045$, Sr >400 ppm, Y < 12 ppm, and Sr/Y > 30 (as per Castillo, 2008; Fig. 2c; Supplementary Fig. S2). The non-adakite nature is also suggested by REE features (Fig. 2d; Supplementary Fig. S2). The investigated frontal arc samples have $^{143}Nd/^{144}Nd$ values ranging from 0.51273 to 0.51283, corresponding to initial ε_{Nd} isotopic values from +2.6 to +4.9. The rear-arc samples have $^{143}Nd/^{144}Nd$ range from 0.51274 to 0.51279, and initial ε_{Nd} values from +2.9 to +4.3. The isotopic values of both frontal- and rear-arc samples align with the enriched range of ocean island basalts (OIBs) and exhibit significantly more radiogenic Sr isotopes and less radiogenic Nd isotopes compared to mid-ocean ridge basalts (MORBs) (*e.g.,* Stracke et al., 2005, and references therein).

4.2. Fe isotope values

The $\delta^{56}Fe$ values of the investigated Eocene to Oligocene frontal arc magmas (*i.e.*, Eshtehard, Saveh, Qom, Natanz, Nodoushan, and Oligocene SE UDMA) define a consistent narrow range (Fig. 3; Appendix Table S1; Supplementary Fig. S4). Indeed, Eshtehard lavas show a range from +0.07 ± 0.05 ‰ to +0.09 ± 0.02 ‰. Saveh lavas range from +0.08 ± 0.05 ‰ to +0.09 ± 0.02 ‰. Qom lavas display values similar to those of Eshtehard (*i.e.,* from +0.07 ± 0.04 ‰ to +0.09 ± 0.02 ‰). Natanz lavas show a range of +0.09 ± 0.05 ‰ to +0.10 ± 0.05 ‰. Nodoushan lavas range from +0.09 ± 0.06 ‰ to +0.11 ± 0.06 ‰. The Oligocene SE UDMA samples show a range of +0.07 ± 0.01 ‰ to +0.12 ± 0.03 ‰ (Babazadeh et al., 2024a). Considered all together, samples from the

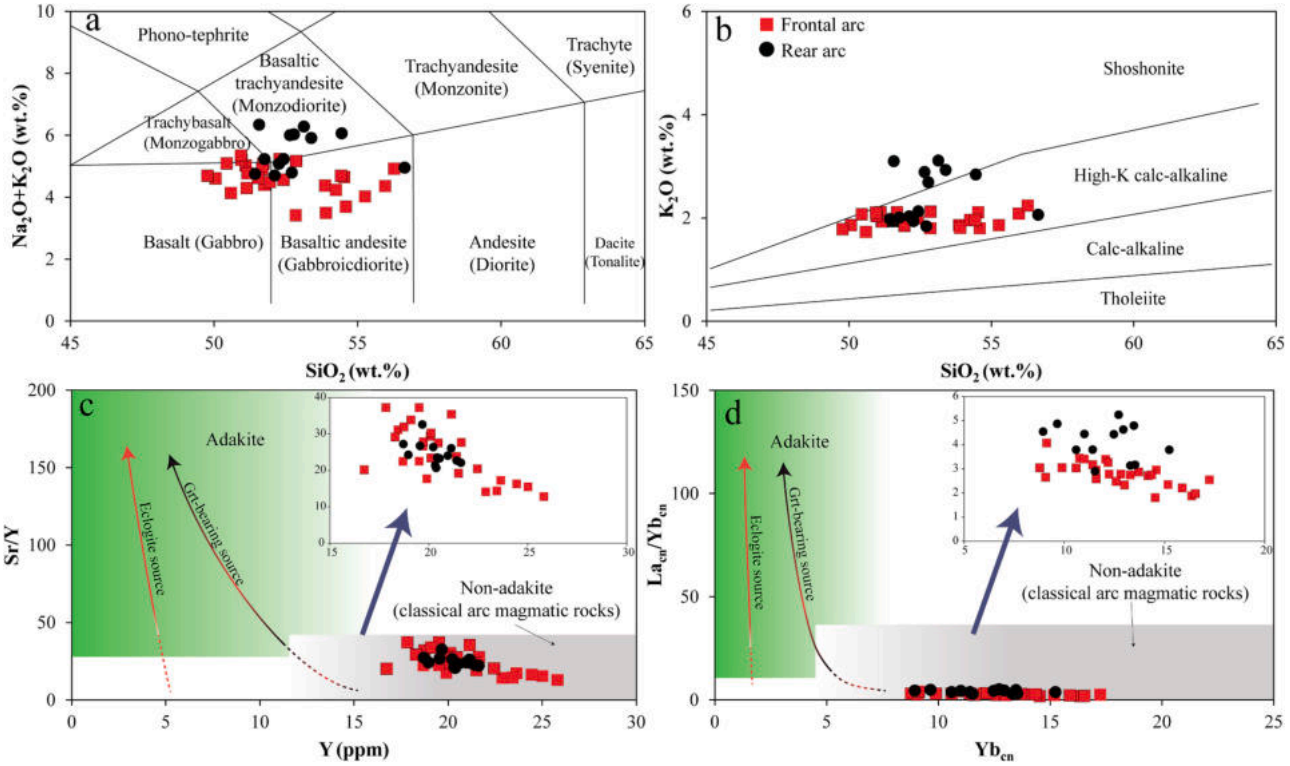

Fig. 2. a) TAS classification diagram (Le Maitre, 2002); b) K_2O *vs.* SiO_2 classification diagram (Peccerillo and Taylor, 1976). Data show high-K signatures; c) Sr/Y *vs.* Y; d) La/Yb *vs.* Yb. The analyzed data plot within the non-adakite (classical arc magmatic rocks) field. Data from Appendix Table S1.

frontal arc give a weighted mean δ^{56}Fe of +0.090 ± 0.006 (2σ) (Appendix Tables S1, S3 and S4; Supplementary Fig. S5).

Compared with the frontal arc samples, the investigated Eocene to Oligocene rear arc magmas equivalents (*i.e.*, Roshtkhar–Torbat-e-Heydarieh, Sabzevar, Moalleman, and Quchan) have higher δ^{56}Fe values (Fig. 3; weighted mean + 0.135 ± 0.010 (2σ); Appendix Tables S1, S3 and S4; Supplementary Figs. S3 and S4). In detail, Eocene Roshtkhar–Torbat-e-Heydarieh lavas range from +0.14 ± 0.08 ‰ to +0.16 ± 0.03 ‰, Sabzevar lavas display a range of +0.14 ± 0.06 ‰ to +0.15 ± 0.03 ‰, Moalleman lavas range from +0.12 ± 0.04 ‰ to +0.13 ± 0.04 ‰, and Oligocene Quchan lavas range from +0.13 ± 0.02 ‰ to +0.14 ± 0.04 ‰. The δ^{56}Fe values of frontal arc samples mimic those of global depleted MORBs, whereas the δ^{56}Fe values of rear arc samples mimic those of global *E*-MORBs and OIBs (Fig. 3; Supplementary Figs. S1 and S4). The δ^{56}Fe data display a positive correlation with increasing silica, with no marked association with ^{143}Nd/^{144}Nd isotopic values (Fig. 4a and b; Supplementary Fig. S6). To better constrain the mechanisms of Fe isotope fractionation in the frontal- and rear-arc settings of Cenozoic magmatism in Iran, the geochemical and Fe—Nd isotopic data reported from SE UDMA (in the frontal arc) were also included (Babazadeh et al., 2024a).

5. Discussion

5.1. Redox conditions

Magmas erupted at subduction zones typically exhibit arc-like compositional characteristics, including high $Fe^{3+}/\Sigma Fe$ values (0.19–0.54), reflecting their oxidized state. These elevated $Fe^{3+}/\Sigma Fe$ values are often associated with subduction-related processes, such as metasomatism by fluids (Brounce et al., 2014; Grocke et al., 2016; Bénard et al., 2018). In contrast, mantle peridotites, which represent the residue left after melt extraction or metasomatic modification, show a wide range of $Fe^{3+}/\Sigma Fe$ values depending on their tectonic setting. For example, mantle peridotites from cratonic or ancient lithospheric settings display relatively low $Fe^{3+}/\Sigma Fe$ values (~0.019). Conversely, peridotites in mid-ocean ridge settings, depleted due to repeated melt extraction, exhibit intermediate $Fe^{3+}/\Sigma Fe$ values (~0.16) (*e.g.*, Canil et al., 1994; Brounce et al., 2014; Grocke et al., 2016). Global arc magmas commonly exhibit δ^{56}Fe values lighter than those of mid-ocean ridge basalts (MORB) (*e.g.*, Liao et al., 2023; Nebel et al., 2013). This isotopic characteristic is notable given that arc magmas generally possess elevated $Fe^{3+}/\Sigma Fe$ ratios relative to the depleted MORB mantle (DMM). Such a trend is counterintuitive in the context of oxidation-driven isotopic fractionation, as Fe^{3+} is both more incompatible and theoretically isotopically heavier than Fe^{2+} (*e.g.*, Dauphas et al., 2014; Williams et al., 2018). The observation that δ^{56}Fe values are lighter despite higher $Fe^{3+}/\Sigma Fe$ ratios suggests that the interplay between oxidation and reduction alone does not govern Fe isotope systematics in these settings and that additional processes and/or components must be involved (*e.g.*, slab-derived fluids, sediment melts, and fractional crystallization).

Mantle wedge peridotites in subduction zones (*e.g.*, Mariana forearc) exhibit high and variable $Fe^{3+}/\Sigma Fe$ ratios (~0.1–0.8), reflecting the influence of slab-derived fluids (*e.g.*, Canil et al., 1994; Parkinson and Arculus, 1999; Birner et al., 2017; Bénard et al., 2018; Debret et al., 2020). However, progressive dehydration alone does not significantly alter Fe oxidation states in mantle melts ($Fe^{3+}/\Sigma Fe < 0.4$; Kelley and Cottrell, 2009; Debret et al., 2020). Instead, oxidation is more effectively driven by multivalent components (*e.g.*, C, S) released from subducting slab, which elevate mantle $Fe^{3+}/\Sigma Fe$ to values >0.5 (*e.g.*, Debret et al., 2020). This process can lead to Fe isotope fractionation, as observed in serpentinites from the Mariana forearc, which show uniform $Fe^{3+}/\Sigma Fe$ (~0.51–0.68) and negative δ^{56}Fe (−0.27 to −0.1 ‰), suggesting steady-state oxidation conditions maintained by fluid activity.

In this scenario, the geochemical signatures of the Iranian frontal- and rear-arc magmas, such as positive δ^{56}Fe (*i.e.*, from ~ +0.07 to ~ +0.16) and the absence of negative correlation between δ^{56}Fe and $Fe^{3+}/$

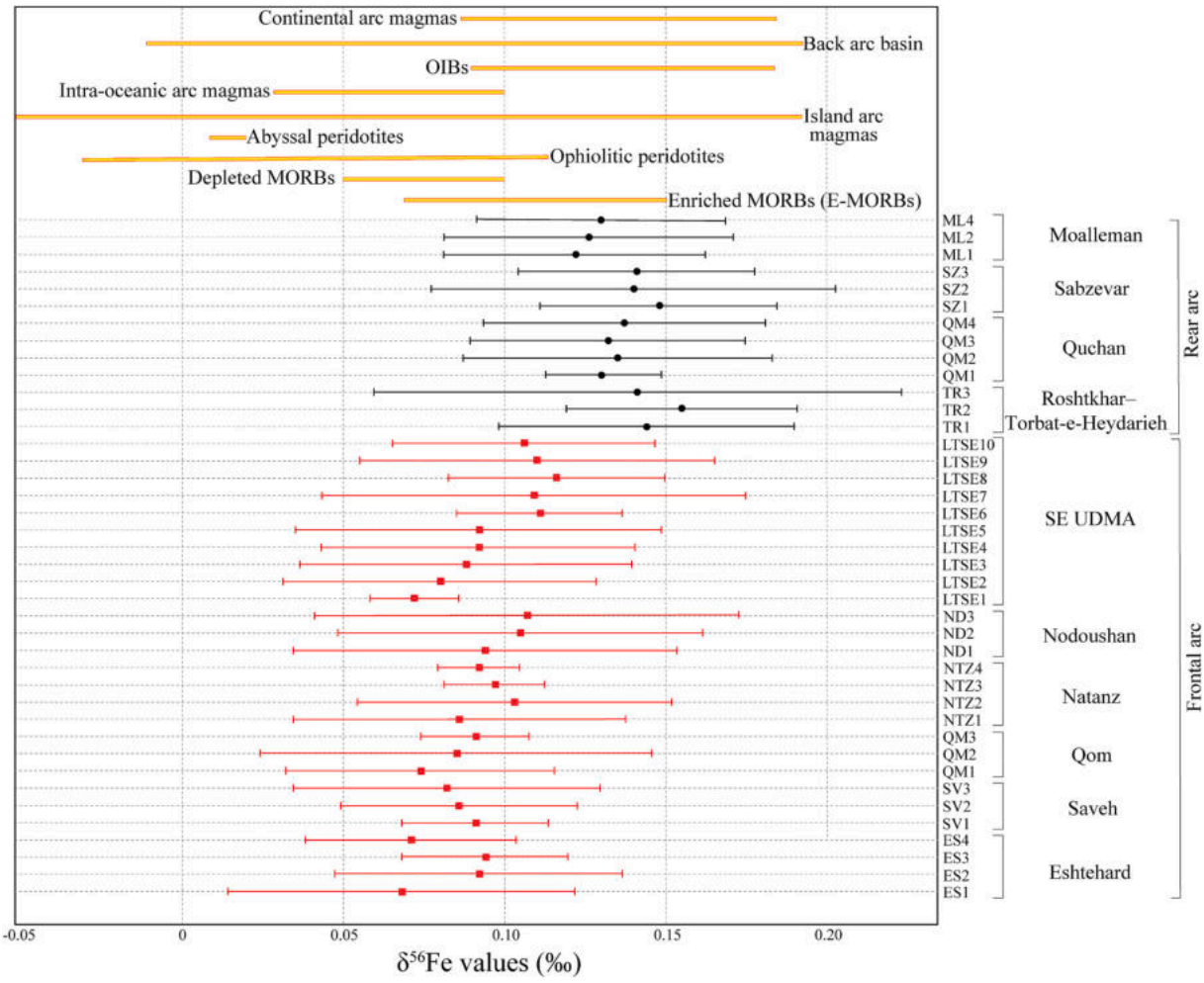

Fig. 3. δ^{56}Fe for frontal- and rear-arc samples, compared to ranges of values for different magmas and mantle sources (references given in the main text). The frontal arc samples exhibit higher δ^{56}Fe values. Data from Appendix Table S1.

ΣFe (Fig. 4c; Supplementary Fig. S6), may indicate that Fe^{3+} might be incorporated into the mantle wedge through a mechanism involving the interaction of slab-derived fluids with mantle minerals, which could modify the oxidation state indirectly by mobilizing redox-sensitive elements.

From a geodynamic point of view, Moghadam et al. (2022b) propose that slab break-off and asthenospheric upwelling, which are associated with Cu-bearing adakitic magmatism, began in the Miocene in the southeastern UDMA. They also suggest that a re-fertilized, hot, and volatile-rich mantle may have been crucial in the formation of porphyry copper deposits (PCDs) in Iran. From a mineralization perspective, several studies (*e.g.*, Raeisi et al., 2021, 2024; Moghadam et al., 2022b; Rabiee et al., 2022; Babazadeh et al., 2024b) have inferred, based on whole rock and zircon geochemical and isotopic data, that the collision between the Arabia and Iran plates resulted in progressive thickening of the continental crust. This would have caused a shift in redox conditions—from reduced to oxidized (high fO_2)— thought to be a key factor in the formation of large, fertile PCDs throughout Iran from Oligocene to Miocene. According to our own geochemical and isotopic findings, the Eocene-Oligocene magmatism observed in both frontal- and rear-arcs (*i.e.*, this study) does not exhibit the geochemical signatures typically associated with Cu production, as documented in various arc-related settings worldwide (*e.g.*, Seedorff et al., 2005; Wang et al., 2006; Tadevosyan et al., 2018; Kuşcu et al., 2019; Simmonds, 2019; Richards, 2022; Zhong et al., 2021; Gao et al., 2023), suggesting a "low-fO_2 barren magmatism" environment.

5.2. Fluid exsolution

Fluid exsolution during magma ascent fractionates Fe isotopes, with Fe preferentially partitioning into the fluid phase (*e.g.*, Beard and Johnson, 2004). However, in arc settings, this effect is typically overwhelmed by slab-derived fluid inputs (*e.g.*, Dauphas and Rouxel, 2006). Previous studies have demonstrated that fluid exsolution can induce subtle yet impactful shifts in Fe isotope ratios, particularly in volatile-rich subduction environments, during magma differentiation and crystallization (*e.g.*, Frost and McCammon, 2008; Shahar et al., 2008). Fluid exsolution significantly decreases Zr/Hf, Nb/Ta, and K/Rb to values less than 26, 5, and 100, respectively, but increases the lanthanide tetrad–effect (*e.g.,* $TE_{1,3} > 1.1$; Ballouard et al., 2016). In Iranian frontal- and back-arc samples, the near-chondritic values of fluid-immobile and fluid-soluble element ratios, *e.g.,* Zr/Hf = 37–56, Nb/Ta = 11–27, K/Rb > 388, and $TE_{1,3} \leq 1$, indicate that slab components are negligible or contribute insignificantly to the Fe isotope fractionation (Fig. 5a–d; Supplementary Fig. S7) reflecting the behavior of fluid-soluble elements during mantle melting. Consequently, the absence of significant variations in these ratios supports the interpretation that slab components do not play a major role in driving the Fe isotope variations observed in these samples.

For the Iranian magmatic rocks, the lack of any clear co-variations of δ^{56}Fe with Rb/La and Ba/La, and the absence of wing-shaped REE profiles (*i.e.,* tetrad effect) indicate insignificant contribution from fluid exsolution (Fig. 6a and b, and Supplementary Figs. S2 and S8). In

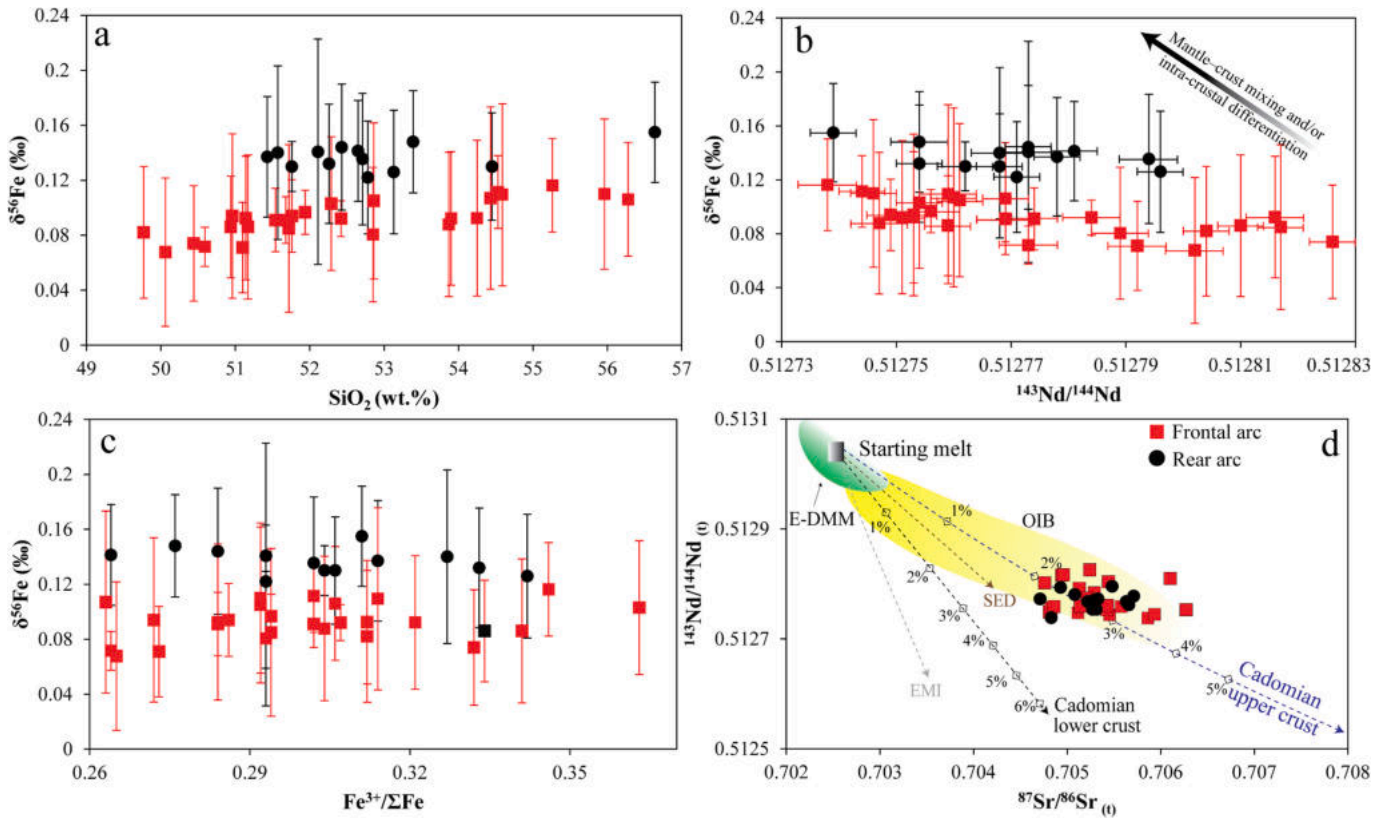

Fig. 4. Binary diagrams of (a) δ^{56}Fe *vs.* SiO_2; (b) δ^{56}Fe *vs.* $^{143}Nd/^{144}Nd$; (c) δ^{56}Fe *vs.* $Fe^{3+}/\Sigma Fe$; and (d) $^{143}Nd/^{144}Nd$ *vs.* $^{87}Sr/^{86}Sr$. Data show slightly increasing in δ^{56}Fe values with magmatic evolution, but no significant contribution of fluid (as inferred from rather constant δ^{56}Fe values *vs.* $Fe^{3+}/\Sigma Fe$), and continental crust (*i.e.,* up to 3 %) on Fe isotope fractionation. Data from Appendix Table S1.

contrast, the data almost follow a trend of sediment addition, similarly to other samples from both the UDMA (*i.e.*, frontal arc; Babazadeh et al., 2023) and NE Iran (*i.e.*, rear arc; Ahmadi et al., 2019; Alizadeh et al., 2023). The incompatible trace element ratios (*e.g.*, Ba/La and Rb/La) and δ^{56}Fe values of the studied regions in Iran plot outside the Mariana intra-oceanic arc field, which is characterized by strong fluid influence and highly oxidized conditions (Kelley et al., 2007; König et al., 2019). Instead, they exhibit greater similarity to the Kamchatka continental arc, where fluid-driven metasomatism is negligible, and oxidation effects are limited (Fig. 6a, b, and Supplementary Fig. S8).

5.3. Intra-crustal differentiation and crustal assimilation

During intra-crustal differentiation of magmatic rocks, processes such as fractional crystallization and assimilation cause different elements to behave in distinct ways. Iron (mostly as Fe^{2+}) is preferentially incorporated into early-formed minerals like olivine, pyroxene, and amphibole, resulting in the gradual depletion of Fe in the melt and increase in δ^{56}Fe values. Conversely, incompatible trace elements like REEs, including neodymium (Nd), remain preferably in the residual melt. However, the behavior of such elements may be variable, due to specific mineral phases fractionating in the course of magma differentiation, since they can be either incorporated into, or excluded from their crystal structure. Even more complex behavior is shown by incompatible trace elements if continental crust is assimilated in concomitance with crystal fractionation. In this case, a negative correlation between Fe and Nd isotopic compositions emerges, given the unradiogenic Nd-isotope feature of continental crust. If the initial-Nd isotope value serves as a "continental crust" tracer, Iranian rear-arc magmas might have higher proportions of assimilant than frontal arc equivalents. However, no meaningful correlation between δ^{56}Fe and initial-Nd isotope ratios is observed (Fig. 4b, d, and Supplementary Fig. S6), arguing for negligible cannibalization of crustal materials following the upward injection of mantle-derived melts (see also Babazadeh et al., 2024a). To further assess the potential impact of crustal contamination, we performed a mass balance mixing model through Sr and Nd isotopes using a starting melt composition intermediate between the lower limit of *E*-DMM (*i.e.,* depleted over the average of DMM) and the upper limit of OIB-like sources, and Iranian Cadomian continental crust as end members. Although we found that crustal contamination is not significant, the modelling serves to quantify the maximum extent of contamination in the frontal- and rear-arc samples. Our modelling reveals low degrees of addition (*i.e.*, 3 % to as little as 2 %; Fig. 4d and Supplementary Fig. S6), which corroborates our interpretation that crustal contamination may not significantly influence the δ^{56}Fe values. Notice that the on average higher Sr/Y ratios in the rear-arc relative to frontal arc data (see Fig. 2c, and Supplementary Fig. S2) may result from the addition of some slab-derived melts to the source, potentially also accounting for the slightly unradiogenic $^{143}Nd/^{144}Nd$ ratio rather than crustal assimilation.

It is noteworthy to mention that a low degree of crustal contamination agrees with a limited crustal thickening. The progress of arc maturity from Eocene to Oligocene and associated crustal thickening apparently failed to drive significant Fe depletion through garnet involvement as inferred from the absence of a systematic change between δ^{56}Fe and Sm/Yb (and Dy/Yb) in both frontal- and rear-arc samples (Supplementary Fig. S9a and b). The pre-collisional frontal- and rear-arc magmas investigated here lack adakitic geochemical signatures, and their formation predates the onset of significant crustal thickening. This feature suggests that the mechanisms responsible for Fe depletion and Cu—Au mineralization in post-collisional adakitic systems were not active during the genesis of these pre-collisional magmas. Instead, their δ^{56}Fe signatures likely reflect mantle source variations and/or magmatic differentiation processes rather than crustal

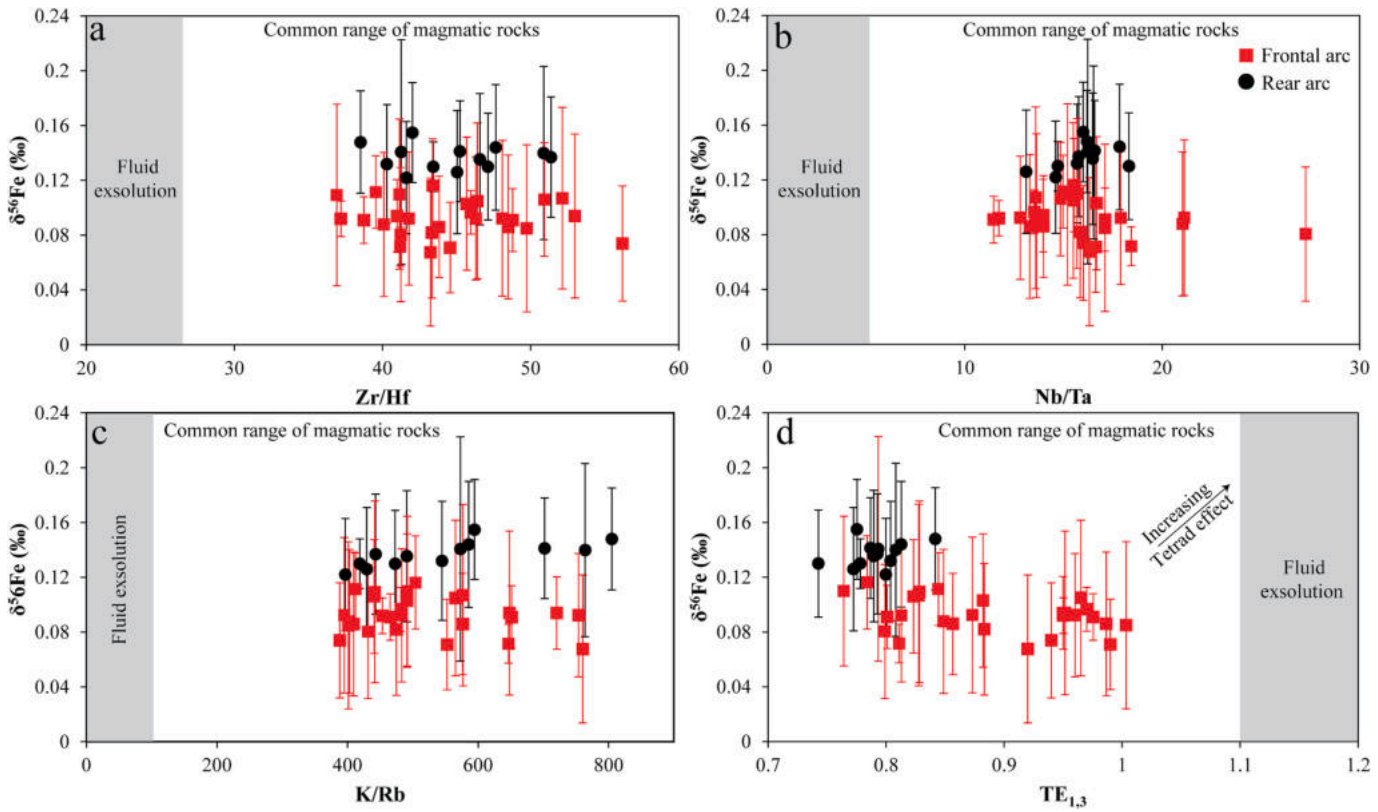

Fig. 5. Binary diagrams illustrating (a) δ^{56}Fe *vs.* Zr/Hf, (b) δ^{56}Fe *vs.* Nb/Ta, (c) δ^{56}Fe *vs.* K/Rb, and (d) δ^{56}Fe *vs.* $TE_{1,3}$ (*i.e.*, the first and third tetrad effects) for the frontal- and rear-arc volcanic rocks from Iran (data compiled in Appendix Table S1). The limited fractionation observed in Zr/Hf, Nb/Ta, and K/Rb ratios (≤10 % deviation from typical magmatic values) indicates minimal fluid-related modification, consistent with contributions from pelitic sediment residues rather than serpentinite-derived slab fluids. The lack of statistically significant correlations between δ^{56}Fe and these elemental ratios ($R^2 < 0.2$) further argues against a substantial slab fluid component.

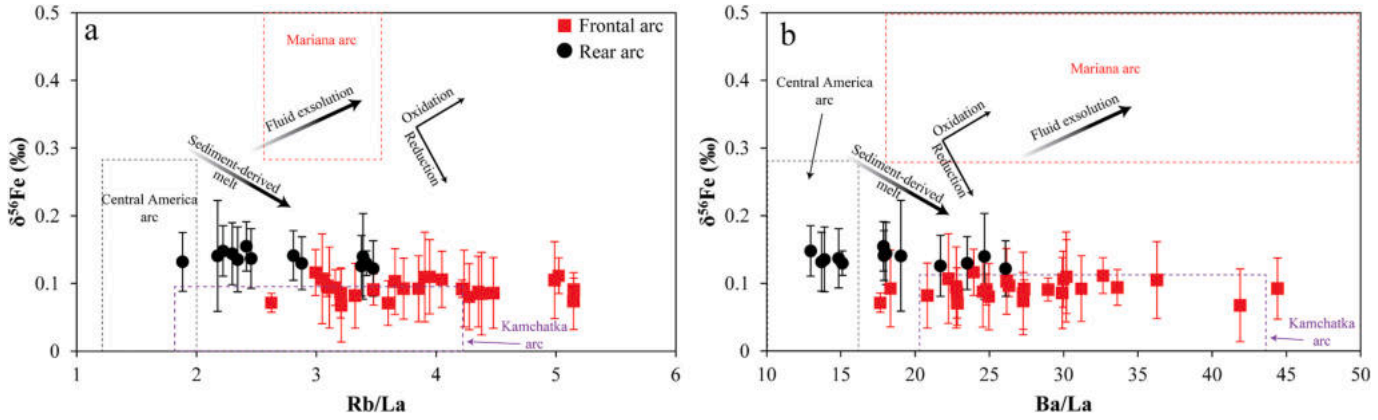

Fig. 6. Binary diagrams of (a) δ^{56}Fe *vs.* Rb/La and (b) δ^{56}Fe *vs.* Ba/La for volcanic rocks from Iran, compared to representative arc systems (Central America, Mariana, and Kamchatka arcs; references given in the main text; data from Appendix Table S1). Illustrative vectors show the expected trends for fluid exsolution and sediment-derived melt. In (a), the δ^{56}Fe values show no correlation with Rb/La ($R^2 < 0.1$), indicating minimal fluid influence, contrasting with the Mariana arc (highly oxidized, fluid-dominated). The data instead align with the Kamchatka continental arc, where fluid metasomatism is negligible (<1 %). In (b), low Ba/La ratios and δ^{56}Fe values further support limited fluid input, as samples plot far from the Mariana arc field. The weak trend suggests either (1) minor fluid release or (2) dominance of source heterogeneity or partial melting processes, consistent with fluid-poor continental arcs like Kamchatka.

thickening-driven fractionation and metal enrichment.

5.4. Mineral-melt fractionation

Previous studies on the arc magmatism of Iran have revealed that clinopyroxene (and/or olivine) are the main, although volumetrically subordinate, ferromagnesian minerals in the Eocene basic suites of the frontal arc (*e.g.*, Yazdani et al., 2018; Nouri et al., 2021; Babazadeh et al., 2021, 2024a; Moradi et al., 2022). In contrast, the rocks representing the rear arc magmatism show larger volumes of ferromagnesian mineral assemblages (*e.g.*, clinopyroxene, olivine, and amphibole) compared to the Eocene frontal arc suites (*e.g.*, Alizadeh et al., 2023; Ahmadi et al., 2024). However, this pattern does not extend to the Oligocene to Miocene suites, where rear arc basic magmatism is

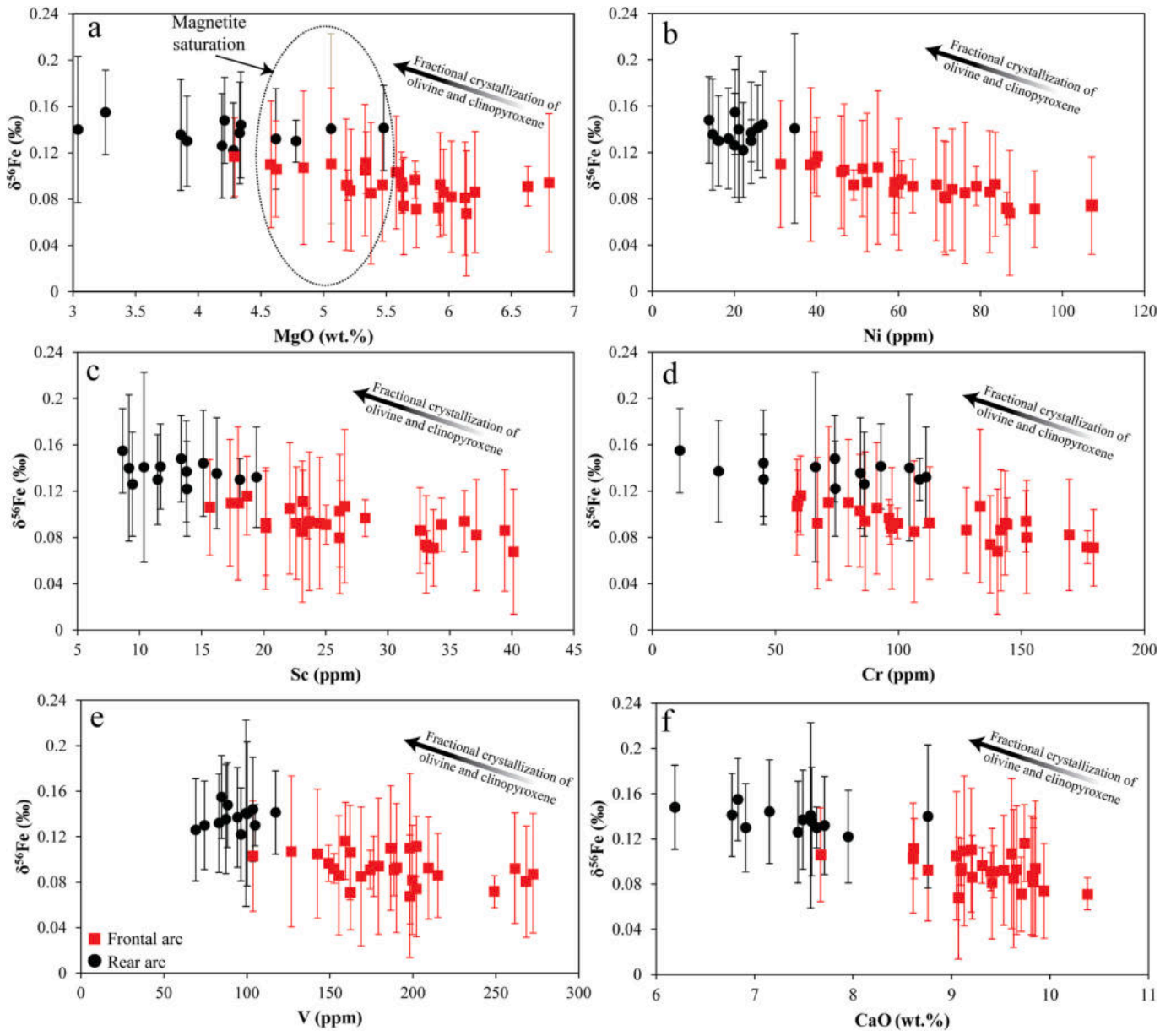

Fig. 7. Binary diagrams of (a) δ^{56}Fe *vs.* MgO; (b) δ^{56}Fe *vs.* Ni; (c) δ^{56}Fe *vs.* Sc; (d) δ^{56}Fe *vs.* Cr; (e) δ^{56}Fe *vs.* V, and (f) δ^{56}Fe *vs.* CaO. Data from Appendix Table S1. Data suggest that fractional crystallization of Fe-bearing phases would result in Fe isotope fractionation in both frontal- and rear-arc magmas.

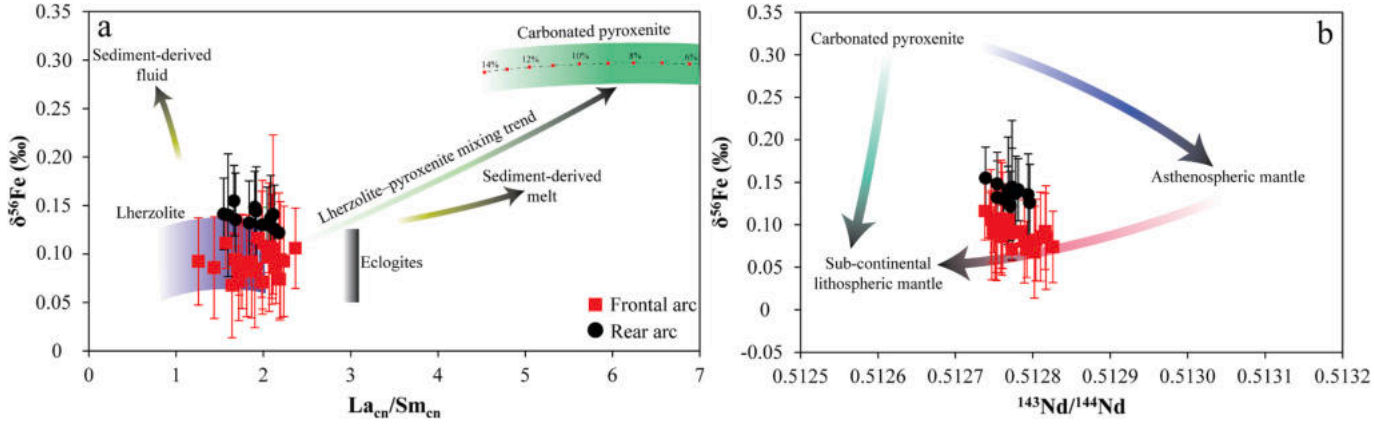

Fig. 8. Variation of δ^{56}Fe as a function of (a) La_{cn}/Sm_{cn}, and (b) $^{143}Nd/^{144}Nd$. Data from Appendix Table S1. The data indicates mixing of melt from asthenospheric mantle and SCLM sources. More details are provided in the main text.

characterized by variable presence of ferromagnesian minerals as compared to their frontal arc counterparts (*e.g.*, Moghadam et al., 2016; Ahmadi et al., 2019; Rostami-Hossouri et al., 2020; Dong et al., 2024). We examine the possibility that the observed Fe isotope fractionation be a result of mineral–melt fractionation during partial melting and crystallization. Isotopic fractionation during partial melting can account for the ~0.1 ‰ shift of δ^{56}Fe in basalts with respect to chondrites and peridotites (*e.g.,* Dauphas et al., 2014). Crystallization and removal of minerals with distinct Fe isotope compositions from the host magmas are responsible for larger shifting of δ^{56}Fe values (*e.g.,* Teng et al., 2008; Sossi et al., 2012; Foden et al., 2018). Fractionation of Fe^{3+}-rich phases in a steady state magma chamber, particularly magnetite, preferentially removes Fe^{3+} from the melt, driving the residual magma toward lighter Fe isotopic compositions. In contrast, Fe^{2+}-rich silicates such as olivine, pyroxene, amphibole, and garnet preferentially incorporate lighter Fe isotopes, leading to enrichment of the residual melt in heavy Fe isotopes upon fractionation (*e.g.,* Sossi et al., 2012; Dauphas et al., 2014). While amphibole can accommodate a higher proportion of Fe^{3+} relative to other Fe—Mg silicates (with $Fe^{3+}/\Sigma Fe \approx 0.25$), it remains an Fe^{2+}-dominant phase. Consequently, its crystallization results in only a minor shift toward lighter Fe isotopic compositions compared to magnetite. Garnet, also predominantly Fe^{2+}-bearing, concentrates lighter Fe isotopes, and its fractionation enriches the residual magma in heavier Fe isotopes. Among these phases, magnetite is the most effective mineral in depleting Fe^{3+} from the melt and plays the main role in shifting Fe isotopic compositions toward lighter values (*e.g.,* Ye et al., 2020). As determined through investigation of various minerals including magnetite of the Upper and Upper Main Zones (UUMZ) of the Bushveld Complex, the δ^{56}Fe composition of various minerals has been analyzed to assess the role of fractional crystallization in controlling the Fe isotopic evolution of a mafic magma (*e.g.,* Bilenker et al., 2017 and references therein). The results are as follows: plagioclase (+0.91 ± 0.33 ‰) > K-feldspar (+0.88 ± 0.16 ‰) > magnetite (+0.29 ± 0.17 ‰) > biotite (+0.07 ± 0.07 ‰) > amphibole (+0.05 ± 0.04) > clinopyroxene (−0.06 ± 0.07 ‰) > olivine (−0.15 ± 0.23 ‰) > ilmenite (−0.23 ± 0.13 ‰).

In this scenario, the crystallization of Fe^{2+}-rich minerals affects the isotopic composition (δ^{56}Fe), but not necessarily the $Fe^{3+}/\sum Fe$ ratio. Fractionation between Fe^{2+} and Fe^{3+} is controlled by the redox state of Fe, which is sensitive to factors like temperature, fO_2, and nature of mineral phases. During crystallization of Fe^{2+}-rich minerals, lighter Fe isotopes preferentially partition into the mineral, causing the δ^{56}Fe of the residual melt to increase (Shahar et al., 2008). In contrast, the $Fe^{3+}/\sum Fe$ ratio, which reflects the system's redox state, primarily responds to changes in fO_2. For redox conditions to influence δ^{56}Fe, iron must be transferred among phases (*e.g.*, fluid–melt or mineral–melt) in which Fe^{2+}/Fe^{3+} partitioning is sensitive to redox conditions. As fO_2 rises, Fe^{3+} increases, but this does not always lead to a corresponding shift in isotopic composition. The decoupling of δ^{56}Fe and $Fe^{3+}/\sum Fe$ underscores that isotopic fractionation is not inherently redox-driven but depends on iron transfer among reservoirs where redox-sensitive partitioning occurs. The isotopic fractionation between Fe^{2+} and Fe^{3+} depends on mineral-specific partitioning, not the bulk $Fe^{3+}/\sum Fe$ ratio (*e.g.*, Dauphas and Rouxel, 2006; Beard et al., 1999). This is evident in low fO_2 systems, where Fe^{2+}-rich mineral crystallization occurs without a significant increase in $Fe^{3+}/\sum Fe$. As a result, the δ^{56}Fe value increases in the melt, independent of the redox state (Frost and McCammon, 2008).

Chondrite-normalized REE profiles of the frontal- and rear-arc magmas show rather flat patterns for the MREE–HREE section (Supplementary Fig. S3), arguing against substantial contribution of garnet fractionation/retention as a plausible reason for lighter Fe depletion. The frontal- and rear-arc samples have Mg# ranging from 53 to 62, and 42 to 56, respectively (Appendix Table S1), which are lower than those reported from the undifferentiated upper mantle melts in equilibrium with residual olivine (*e.g.,* Mg# ~ 74, Fo_{90}) (*e.g.,* Sossi et al., 2012). Moreover, the samples have <272 ppm V, <107 ppm Ni, <40 ppm Sc, and < 179 ppm Cr (Appendix Table S1), augmenting the inference that these lavas do not reflect primary magma compositions but have undergone substantial fractionation of liquidus minerals concentrating light δ^{56}Fe (*e.g.,* olivine and clinopyroxene). In that respect, the rear arc basalts experienced on average higher extent of fractionation prior to eruption, which also aligns with MgO, CaO and compatible trace elements variation diagrams (Fig. 7, and Supplementary Fig. S10). Therefore, fractional crystallization of olivine and clinopyroxene would be a suitable process resulting in the observed Fe isotope fractionation in both frontal- and rear-arc magmas.

5.5. Source melting and tectono-magmatic setting

While residual peridotite resulting from melt extraction typically exhibits elevated δ^{56}Fe values—owing to the preferential partitioning of light Fe isotopes (^{54}Fe) into silicate melts—carbonated pyroxenite can develop equally enriched, or even higher, δ^{56}Fe signatures through three synergistic mechanisms. First, carbonate-induced metasomatism elevates oxygen fugacity (fO_2), promoting the oxidation of Fe^{2+} to Fe^{3+} in mineral phases such as garnet and amphibole, which strongly fractionate Fe isotopes toward heavier values (*e.g.*, Poitrasson et al., 2013; Sossi et al., 2016). Second, pyroxenites that crystallize as cumulates rather than from equilibrium melts preferentially retain high-δ^{56}Fe minerals (*e.g.*, clinopyroxene, garnet), whereas melt-depleted peridotite—dominated by olivine and orthopyroxene with lower Fe isotope fractionation capacity—may not achieve similar levels of isotopic enrichment. Third, in sulfur-bearing systems, sulfide precipitation preferentially incorporates light Fe isotopes, thereby enriching the residual pyroxenite in heavier δ^{56}Fe values (*e.g.*, Dauphas et al., 2017). Thus, although peridotite residues are generally characterized by higher δ^{56}Fe than melts derived from pyroxenitic sources, carbonated pyroxenites can exceed lherzolite in δ^{56}Fe under conditions where (i) crystallization occurs at elevated fO_2, (ii) cumulate textures are preserved, or (iii) garnet and sulfide phases are present. This systematics provide a robust framework for interpreting heavy δ^{56}Fe signatures in mantle-derived magmas—particularly those sourced from carbonated domains—and underscore the critical role of redox-sensitive mineralogy in governing Fe isotope behavior during mantle metasomatism.

Building on the empirical modelling of Guo et al. (2023), 1 %–20 % partial melting of a peridotite produces melts with δ^{56}Fe values ranging from +0.04 ‰ to +0.12 ‰, and less-evolved La_{cn}/Sm_{cn} values (*i.e.,* 0.8 to 2.2) than melting of either an eclogite derived from recycled ocean crust or metasomatic garnet pyroxenite (δ^{56}Fe − 0.2 ‰ to +0.3 ‰ and La_{cn}/Sm_{cn} 0.5–1, and δ^{56}Fe + 0.24 ‰ to +0.32 ‰ and La_{cn}/Sm_{cn} 4.2–7, respectively). Moreover, geochemical and Fe—Nd isotopic investigations on the Northern Lau Basin–a rear-arc basin located in the southwest Pacific– revealed that a pyroxenitic component in their mantle source increases the δ^{56}Fe values up to +0.34 ‰ (*e.g.*, Konter et al., 2016). The frontal- and rear-arc whole rock geochemistry and Fe isotopic data of the investigated samples from Iran preclude partial melting of either eclogite or carbonated pyroxenite sources and instead suggest melting of a heterogeneous garnet-free peridotite with low abundances and ratios of incompatible elements (Fig. 8a, and Supplementary Fig. S11). This interpretation stands in marked contrast to the model recently proposed by Ahmadi et al. (2024), which attributes the geochemical signatures of rear-arc magmatism in Iran to parental melts derived from a pyroxenitic mantle source.

In continental arcs like the Zagros, rear-arc magmatism reflects hybrid sources: metasomatized lithosphere and asthenospheric melts (*e.g.*, Moghadam et al., 2023). This differs from oceanic rear-arcs (*e.g.*, Lau Basin) where extension drives melting from a MORB-like source (*e.g.*, Konter et al., 2016). As illustrated in the δ^{56}Fe *vs.* $^{143}Nd/^{144}Nd$ diagram (Fig. 8b) the investigated Cenozoic data follow a trend of asthenosphere–subcontinental lithosphere source mixing, ruling out once again a role for melting of eclogite or pyroxenite sources.

Regarding the yielded δ^{56}Fe values of the investigated magmas (see Fig. 3 and Supplementary Fig. S4), it is plausible that the pre-collisional

magmatism of frontal- and rear-arcs may have developed in conjunction with Neo-Tethyan slab steepening and rollback which triggered asthenospheric upwelling. The resulting magmas, derived from a source region intermediate to those of *E*-MORB-like and the upper limit of OIB-like mafic rocks, were affected by interaction between melts of asthenosphere and metasomatized peridotite.

The Fe isotope systematics observed in the Iranian segment of the Neo-Tethys subduction system reveal subtle yet significant distinctions between frontal- and rear-arc magmas. Foden et al. (2018) demonstrated that back-arc magmas in extending rift systems (*e.g.*, western Pacific) where slab rollback and lithospheric extension promote decompression melting in an oxidized mantle wedge, quickly evolve from lighter arc-like to heavier MORB-like δ^{56}Fe ($\sim +0.15$ ‰). While our rear-arc samples show heavier δ^{56}Fe than frontal arc ($+0.135 \pm 0.010$ ‰), they remain distinct from MORB, implying limited slab rollback and intra-arc rifting in the Zagros. This pattern aligns with global trends in rear-arc geochemistry. Rear arc samples from northeastern Iran exhibit heavier δ^{56}Fe values than their frontal arc counterparts ($+0.090 \pm 0.006$ ‰), a pattern consistent with observations from other subduction zones where rear-arc magmas commonly show heavier Fe isotopes, possibly due to differences in redox conditions during melting. The δ^{56}Fe values in the Iranian rear-arc likely result from a combination of reduced slab-derived fluid influence, greater degrees of asthenospheric melting, and deeper fractional crystallization of Fe^{2+}-rich phases, such as clinopyroxene. Unlike the extensive rifting observed in the western Pacific (*e.g.*, Lau Basin; Konter et al., 2016), the Iranian rear-arc appears to reflect localized extension without significant lithospheric thinning in Eocene (*i.e.*, the absence of full intra-arc rifts conditions). These findings support a geodynamic scenario in which Iranian rear arc magmatism represents a transitional regime shaped by incipient extensional processes superimposed on a subduction-modified mantle source, consistent with the continued slab rollback during the Oligocene along the Neo-Tethyan margin (*e.g.*, Babazadeh et al., 2017, 2023; Moghadam et al., 2022b). However, our findings on the investigated pre-collisional settings are likely not representative of the entire Neo-Tethyan realm, since the geodynamic evolution of the Zagros orogen (along with the Pontides and Lesser Caucasus) has undergone significant changes from Oligocene onward, in the post-collisional period.

6. Conclusion

This is the first comprehensive report of Fe isotope values in Cenozoic frontal- and rear-arc magmatic rocks of Iran. The data show variation in δ^{56}Fe values from $+0.07 \pm 0.04$ ‰ to $+0.16 \pm 0.03$ ‰, low $Fe^{3+}/\Sigma Fe$ (*i.e.,* ~0.26 to ~0.36), and mantle-dominant signatures as inferred from positive initial-Nd isotopic values (*i.e.,* $\varepsilon_{Nd} + 2.6$ to $+4.9$). Rear arc rocks show slightly higher δ^{56}Fe values than frontal arc rocks (weighted mean $+ 0.135 \pm 0.010$ *vs.* $+0.090 \pm 0.006$). The poorly evolved La_{cn}/Sm_{cn} values of the investigated samples are in marked contrast to the signatures expected for partial melting of eclogite or metasomatized peridotite (*i.e.,* source heterogeneity), making these lithologies unlikely sources for elevated δ^{56}Fe values. This study reveals that Fe isotope evolution in the Zagros orogen is primarily controlled by fractional crystallization of Fe^{2+}-rich phases (*i.e.,* olivine and clinopyroxene), with rear-arc magmas recording heavier δ^{56}Fe values due to a more oxidized melting context, where Fe^{3+}-rich phases like magnetite could become stable, and/or a slightly greater depth of crystallization that enables clinopyroxene accumulation or retention, and/or extended differentiation. Although redox conditions theoretically influence Fe isotope fractionation (*e.g.*, magnetite crystallization in oxidized melts), the lack of remarkable $Fe^{3+}/\Sigma Fe$-δ^{56}Fe correlation and consistently low oxidation states ($Fe^{3+}/\Sigma Fe < 0.36$) suggest that a "highly oxidized magmatic" context is unlikely to be the primary driver of Fe isotopic fractionation in these pre-collisional magmas. Instead, the bulk Fe isotopic composition of parent melts—inherited from a garnet-free lherzolite source—and subsequent mineral-melt partitioning (*e.g.*, olivine and pyroxene) were the dominant controls. This contrasts with arcs where significant slab fluids or crustal assimilation induce redox-related δ^{56}Fe shifts. In the Zagros, the absence of remarkable magnetite fractionation and the modest δ^{56}Fe range imply that the observed variations are better explained by fractional crystallization of Fe^{2+}-phases under moderately oxidized conditions. Thus, while redox processes cannot be entirely dismissed, their influence appears subordinate to crystal fractionation in this area.

CRediT authorship contribution statement

Shahrouz Babazadeh: Writing – review & editing, Writing – original draft, Visualization, Validation, Supervision, Software, Resources, Project administration, Methodology, Investigation, Funding acquisition, Formal analysis, Data curation, Conceptualization. **Yajun An:** Writing – review & editing, Resources, Methodology, Investigation, Funding acquisition, Formal analysis, Data curation, Conceptualization. **M. Santosh:** Writing – review & editing, Visualization, Validation, Resources, Project administration, Methodology, Investigation, Funding acquisition, Formal analysis, Data curation, Conceptualization. **Tanya Furman:** Writing – review & editing, Visualization, Validation, Supervision, Resources, Methodology, Investigation, Data curation, Conceptualization. **Davood Raeisi:** Writing – review & editing, Visualization, Validation, Resources, Methodology, Investigation, Data curation, Conceptualization. **Behnam Gholipour:** Writing – review & editing, Visualization, Validation, Methodology, Investigation, Data curation, Conceptualization. **Massimo D'Antonio:** Writing – review & editing, Supervision.

Declaration of competing interest

The authors declare that they have no known competing financial interests or personal relationships that could have appeared to influence the work reported in this paper.

Acknowledgment

SB expresses his gratitude to the Natural Science Research Institute at Chungnam National University for their unwavering support during his stay in South Korea. The authors collectively express their appreciation to staff at Institute of Mineral Resources, Chinese Academy of Geological Sciences, Beijing for their contribution on the arrangements of isotopic data. We collectively express our gratitude to two anonymous reviewers whose comments have strengthened the original version of the manuscript, and to Dr. Sonja Aulbach for her additional comments, suggestions and excellent editorial handling.

Appendix A. Supplementary data

Supplementary data to this article can be found online at https://doi.org/10.1016/j.chemgeo.2025.122961.

Data availability

We have shared our data as an uploaded Excel file with appendix tables

References

Ahmadi, P., Ghorbani, M.R., Coltorti, M., Kuritani, T., Cai, Y., Fioretti, A.M., Braschi, E., Giacomoni, P.P., Aghabazaz, F., Babazadeh, S., Conticelli, S., 2019. High-Nb hawaiite-mugearite and high-Mg calc-alkaline lavas from northeastern Iran: Oligo-Miocene melts from modified mantle wedge. Int. Geol. Rev. 61, 150–174.

Ahmadi, P., Ghorbani, M.R., Ghorbani, K., Anderson, J.L., Kuritani, T., Akbari, M., 2024. Eocene mafic alkaline volcanism in north Central Iran: signatures of development and subsequent melting of a pyroxenite mantle source. Lithos 366, 107626.

Alizadeh, E., Li, H., Babazadeh, S., Ma, C., Förster, M.W., 2023. Late Eocene slab retreat, extension, and mantle upwelling inferred from mantle signatures in potassium-rich magmatism in NE Iran. Int. Geol. Rev. 65 (9), 1586–1600.
An, Y., Wu, F., Xiang, Y., Nan, X., Yu, X., Yang, J., Yu, H., Xie, L., Huang, F., 2014. High-precision Mg isotope analyses of low-Mg rocks by MC-ICP-MS. Chem. Geol. 390, 9–21.
Babazadeh, S., Ghorbani, M.R., Bröcker, M., D'Antonio, M., Cottle, J., Gebbing, T., Mazzeo, F.C., Ahmadi, P., 2017. Late Oligocene-Miocene mantle upwelling and interaction inferred from mantle signatures in gabbroic to granitic rocks from the Urumieh–Dokhtar arc, south Ardestan, Iran. Int. Geol. Rev. 59, 1590–1608.
Babazadeh, S., D'Antonio, M., Cottle, J.M., Ghalamghash, J., Raeisi, D., An, Y., 2021. Constraints from geochemistry, zircon U–Pb geochronology and Hf–Nd isotopic compositions on the origin of Cenozoic volcanic rocks from central Urumieh–Dokhtar magmatic arc, Iran. Gondwana Res. 90, 27–46.
Babazadeh, S., Haase, K., Ghalamghash, J., Regelous, M., Poujol, M., Raeisi, D., Zhao, M., 2023. Magmatic evolution of the migrating central Urumieh–Dokhtar arc, Iran: implications for magma production. Int. J. Earth Sci. 112 (5), 1577–1597.
Babazadeh, S., Ghalamghash, J., Raeisi, D., Santosh, M., Furman, T., Choi, S.H., D'Antonio, M., Heilimo, E., Cottle, J.M., 2024a. Arc magmatism associated with continental convergence in the SE segment of the UDMA, Iran: insights from zircon geochronology and Hf–Sr–Nd–Fe isotopes. Lithos 466–467, 107468.
Babazadeh, S., Raeisi, D., Santosh, M., Furman, T., Choi, S.H., D'Antonio, M., 2024b. The spatial–temporal evolution of Neotethyan subduction in central to Southeast Iran: constraints from geochemistry, zircon U–Pb–Hf, and Sr–Nd–Pb isotopes. Chem. Geol. 662, 122247.
Ballouard, C., Poujol, M., Boulvais, P., Branquet, Y., Tartèse, R., Vigneresse, J.L., 2016. Nb-Ta fractionation in peraluminous granites: a marker of the magmatic-hydrothermal transition. Geology 44, 231–234.
Beard, B.L., Johnson, C.M., 2004. Inter-mineral Fe isotope variations in mantle-derived rocks and implications for the Fe geochemical cycle. Geochim. Cosmochim. Acta 68 (22), 4727–4743.
Beard, B.L., Johnson, C.M., Cox, L.M., 1999. Iron isotope variations in meteorites. Geochim. Cosmochim. Acta 63 (19), 2937–2948.
Bénard, A., Klimm, K., Woodland, A.B., Arculus, R.J., Wilke, M., Botcharnikov, R.E., Shimizu, N., Nebel, O., Rivard, C., Ionov, D.A., 2018. Oxidising agents in sub-arc mantle melts link slab devolatilisation and arc magmas. Nat. Commun. 9, 3500. https://doi.org/10.1038/s41467-018-05804-2.
Berberian, F., Berberian, M., 1981. Tectono–plutonic episodes in Iran. In: Gupta, H.K., Delany, F.M. (Eds.), Zagros, Hindukosh, Himalaya Geodynamic Evolution. AGU, Washington D.C., pp. 5–32
Bilenker, L.D., Vantongeren, J.A., Lundstrom, C.C., Simon, A.C., 2017. Iron isotopic evolution during fractional crystallization of the uppermost Bushveld complex layered mafic intrusion. Geochem. Geophys. Geosyst. 18 (3), 956–972.
Birner, S.K., Warren, J.M., Cottrell, E., Davies, F.A., Kelley, K.A., Falloon, T.J., 2017. Forearc peridotites from Tonga record heterogeneous oxidation of the mantle following subduction initiation. J. Petrol. 58 (9), 1755–1780.
Brounce, M.N., Kelley, K.A., Cottrell, E., 2014. Variations in $Fe^{3+}/\Sigma Fe$ of Mariana arc basalts and mantle wedge fO_2. J. Petrol. 55, 2513–2536.
Canil, D., O'Neill, H.S.C., Pearson, D.G., Rudnick, R.L., McDonough, W.F., Carswell, D.A., 1994. Ferric iron in peridotites and mantle oxidation states. Earth Planet. Sci. Lett. 123, 205–230.
Castillo, P.R., 2008. Origin of the adakite–high-Nb basalt association and its implications for postsubduction magmatism in Baja California, México. Geol. Soc. Am. Bull. 120, 451–462.
Chen, Y.-X., Lu, W., He, Y., Schertl, H.-P., Zheng, Y.-F., Xiong, J.-W., Zhou, K., 2019. Tracking Fe mobility and Fe speciation in subduction zone fluids at the slab-mantle interface in a subduction channel: a tale of whiteschist from the Western Alps. Geochim. Cosmochim. Acta 267, 1–16.
Chen, Y., Niu, Y., Duan, M., Gong, H., Guo, P., 2021. Fractional crystallization causes the iron isotope contrast between mid-ocean ridge basalts and abyssal peridotites. Commun. Earth Environ. 2 (1), 65.
Chiu, H.Y., Chung, S.L., Zarrinkoub, M.H., Mohammadi, S.S., Khatib, M.M., Lizuka, Y., 2013. Zircon U–Pb age constraints from Iran on the magmatic evolution related to Neotethyan subduction and Zagros orogeny. Lithos 162–163, 162–187.
Dauphas, N., Rouxel, O.J., 2006. Hf–W and Fe isotopes: the case of Earth's accretion and differentiation. Geochim. Cosmochim. Acta 70 (19), 4799–4811.
Dauphas, N., Craddock, P.R., Asimow, P.D., Bennett, V.C., Nutman, A.P., Ohnenstetter, D., 2009. Iron isotopes may reveal the redox conditions of mantle melting from Archean to present. Earth Planet. Sci. Lett. 288 (1), 255–267.
Dauphas, N., Roskosz, M., Alp, E.E., Neuville, D.R., Hu, M.Y., Sio, C.K., Tissot, F.L.H., Zhao, J., Tissandier, L., Médard, E., Cordier, C., 2014. Magma redox and structural controls on iron isotope variations in Earth's mantle and crust. Earth Planet. Sci. Lett. 398, 127–140.
Dauphas, N., John, S.G., Rouxel, O., 2017. Iron isotope systematics. Rev. Mineral. Geochem. 82 (1), 415–510.
Debret, B., Reekie, C.D.J., Mattielli, N., Beunon, H., Ménez, B., Savov, I.P., Williams, H. M., 2020. Redox transfer at subduction zones: insights from Fe isotopes in the Mariana forearc. Geochem. Perspect. Lett. 12, 46–51.
Dong, X.-H., Wang, S.-J., Pang, K.-N., Shen, J., Chen, Y.-X., Rostami-Hossouri, M., Ghasemi, H., 2024. The behavior of nickel isotopes during mantle melting. Geochim. Cosmochim. Acta 366, 34–44.
Foden, J., Sossi, P.A., Nebel, O., 2018. Controls on the iron isotopic composition of global arc magmas. Earth Planet. Sci. Lett. 494, 190–201.
Frost, D.J., McCammon, C.A., 2008. The redox state of Earth's mantle. Annu. Rev. Earth Planet. Sci. 36, 389–420.
Gao, R., Li, J., Kerr, A.C., Wu, T., Xiao, L., Wang, G., He, X., 2023. Subducted oceanic slab break-off in a post-collisional setting: constraints from petrogenesis of Late Carboniferous dykes in central West Junggar, Xinjiang, NW China. Geol. Mag. 160 (9), 1711–1741.
Grocke, S.B., Cottrell, E., de Silva, S., Kelley, K.A., 2016. The role of crustal and eruptive processes versus source variations in controlling the oxidation state of iron in Central Andean magmas. Earth Planet. Sci. Lett. 440, 92–104.
Guo, P., Niu, Y., Chen, S., Duan, M., Sun, P., Chen, Y., Gong, H., Wang, X., 2023. Low-degree melt metasomatic origin of heavy Fe isotope enrichment in the MORB mantle. Earth Planet. Sci. Lett. 601, 117892.
Heimann, A., Beard, B.L., Johnson, C.M., 2008. The role of volatile exsolution and sub-solidus fluid/rock interactions in producing high $^{56}Fe/^{54}Fe$ ratios in silicic igneous rocks. Geochim. Cosmochim. Acta 72 (18), 4379–4396.
Hofmann, A.W., 1997. Mantle geochemistry: the message from oceanic volcanism. Nature 385, 219–229.
Huang, F., Zhang, Z., Lundstrom, C.C., Zhi, X., 2011. Iron and magnesium isotopic compositions of peridotite xenoliths from Eastern China. Geochim. Cosmochim. Acta 75 (12), 3318–3334.
Huang, J., Guo, S., Jin, Q.-Z., Huang, F., 2020. Iron and magnesium isotopic compositions of subduction-zone fluids and implications for arc volcanism. Geochim. Cosmochim. Acta 278, 376–391.
Kelley, K.A., Cottrell, E., 2009. Water and the oxidation state of subduction zone magmas. Science 325 (5940), 605–607.
Kelley, K.A., Plank, T., Cottrell, E., 2007. The role of fluids in arc volcanism: insights from the Mariana arc. Earth Planet. Sci. Lett. 259, 183–193.
König, S., Eickmann, B., Zack, T., Yierpan, A., Wille, M., Taubald, H., Schoenberg, R., 2019. Iron isotope systematics in subduction zones: new insights from the Kurile and Kamchatka arcs. Geochim. Cosmochim. Acta 265, 510–525.
Konter, J.G., Kelemen, P.B., Houghton, R.W., O'Hara, M.J., 2016. Iron isotope variability in ocean floor lavas and mantle sources in the Lau back-arc basin. Geochim. Cosmochim. Acta 190, 283–298.
Kuşcu, İ., Tosdal, R.M., Gençalioğlu-Kuşcu, G., 2019. Episodic porphyry Cu (-Mo-Au) formation and associated magmatic evolution in Turkish Tethyan collage. Ore Geol. Rev. 106, 125–145.
Le Maitre, R.W. (Ed.), 2002. Igneous Rocks a Classification and Glossary of Terms - Recommendations of the International Union of Geological Sciences, Sub-Commission on the Systematics of Igneous Rocks. Cambridge University Press, pp. 1–236.
Li, J., Tang, S.-H., Zhu, X.-K., Pan, C.-X., 2017. Production and certification of the reference material GSB 04-3258-2015 as a $^{143}Nd/^{144}Nd$ isotope ratio. Geostand. Geoanal. Res. 41 (2), 255–262.
Liao, R., Zhu, H., Li, C., Liu, H., Sun, W., 2023. Iron isotope heterogeneity in magmas of subduction zones and its origin. Lithos 458–459, 107360.
McCoy-West, A.J., Millet, M.-A., Nowell, G.M., Wohlers, A., Wood, B.J., Burton, K.W., 2019. Extensive melting of a depleted mantle reservoir at the Iceland plume. Earth Planet. Sci. Lett. 521, 136–147.
McQuarrie, N., van Hinsbergen, D.J.J., 2013. Retrodeforming the Arabia–Eurasia collision zone: age of collision versus magnitude of continental subduction. Geology 41, 315–318.
Moghadam, H.S., Rossetti, F., Lucci, F., Chiaradia, M., Gerdes, A., Martinez, M.L., Ghorbani, G., Nasrabady, M., 2016. The calc-alkaline and adakitic volcanism of the Sabzevar structural zone (NE Iran): implications for the Eocene magmatic flare-up in Central Iran. Lithos 248, 517–535.
Moghadam, H.S., Griffin, W.L., Santos, J.F., Chen, R.X., Karsli, O., Lucci, F., Sepidbar, F., O'Reilly, S.Y., 2022a. Geochronology, geochemistry and petrology of the Oligocene magmatism in SE segment of the UDMB, Iran. Lithos 416–417, 106644.
Moghadam, H.S., Li, Q.L., Griffin, W.L., Stern, R.J., Santos, J.F., Ducea, M.N., Ottley, C. J., Karsli, O., Sepidbar, F., O'Reilly, S.Y., 2022b. Temporal changes in subduction- to collision-related magmatism in the Neotethyan orogen: the Southeast Iran example. Earth Sci. Rev. 226, 103930.
Moghadam, H.S., Li, Q.L., Li, X.H., Chiaradia, M., Karsli, O., Hoernle, K.A., Griffin, W.L., 2023. Mantle-derived high-K magmatic fluxes in northeast Iran arc: constraints from zircon U–Pb–O–Hf and bulk rock major-trace elements and Sr–Nd–Pb isotopes. Gondwana Res. 119, 1–26.
Moradi, S., Christiansen, E.H., Jiang, S.Y., Ghorbani, M.R., 2022. Petrogenesis and tectonic implications of Cenozoic mafic volcanic rocks in the Kahak area of central Urumieh- Dokhtar magmatic arc, Iran. J. Asian Earth Sci. 239, 105404.
Nebel, O., Arculus, R.J., Sossi, P.A., Jenner, F.E., Whan, T.H.E., 2013. Iron isotopic evidence for convective resurfacing of recycled arc front mantle beneath back arc basins. Geophys. Res. Lett. 40 (22), 5849–5853.
Nebel, O., Sossi, P.A., Bénard, A., Wille, M., Vroon, P.Z., Arculus, R.J., 2015. Redox-variability and controls in subduction zones from an iron-isotope perspective. Earth Planet. Sci. Lett. 432, 142–151.
Nebel, O., Sossi, P.A., Bénard, A., Arculus, R.J., Yaxley, G.M., Woodhead, J.D., Davies, D. R., Ruttor, S., 2019. Reconciling petrological and isotopic mixing mechanisms in the Pitcairn mantle plume using stable Fe isotopes. Earth Planet. Sci. Lett. 521, 60–67.
Nouri, F., Azizi, H., Asahari, Y., Stern, R., 2021. A new perspective on Cenozoic calc-alkaline and shoshonitic volcanic rocks, eastern Saveh (Central Iran). Int. Geol. Rev. 63 (4), 476–503.
Pang, K.N., Chung, S.L., Zarrinkoub, M.H., Lin, Y.C., Lee, H.Y., Lo, C.H., Khatib, M.M., 2013. Iranian ultrapotassic volcanism at ~11 Ma signifies the initiation of post-collisional magmatism in the Arabia–Eurasia collision zone. Terra Nova 25, 405–413.
Parkinson, I.J., Arculus, R.J., 1999. The redox state of subduction zones: insights from arc-peridotites. Chem. Geol. 160 (4), 409–423.

Pearce, J.A., Peate, D.W., 1995. Tectonic implications of the composition of the volcanic arc magmas. Annu. Rev. Earth Planet. Sci. 23, 251–285.
Peccerillo, A., Taylor, S.R., 1976. Geochemistry of Eocene calc-alkaline volcanic rocks from the Kastamonu area, Northern Turkey. Contrib. Mineral. Petrol. 58, 63–81.
Pirouz, M., Avouac, J.P., Hassanzadeh, J., Kirschvink, J.L., Bahroudi, A., 2017. Early Neogene foreland of the Zagros, implications for the initial closure of the Neo-Tethys and kinematics of crustal shortening. Earth Planet. Sci. Lett. 477, 168–182.
Poitrasson, F., Freydier, R., 2005. Heavy iron isotope composition of granites determined by high resolution MC-ICP-MS. Chem. Geol. 222, 132–147.
Poitrasson, F., Delpech, G., Grégoire, M., 2013. On the iron isotope heterogeneity of lithospheric mantle xenoliths: implications for mantle metasomatism, the origin of basalts and the iron isotope composition of the Earth. Contrib. Mineral. Petrol. 165, 1243–1258.
Rabiee, A., Rossetti, F., Lucci, F., Lustrino, M., 2022. Cenozoic porphyry and other hydrothermal ore deposits along the South Caucasus-West Iranian tectono-magmatic belt: a critical reappraisal of the controlling factors. Lithos 430–431, 106874.
Raeisi, D., Zhao, M., Babazadeh, S., Long, L.E., Hajsadeghi, S., Modabberi, S., 2021. Synthesis on productive, sub productive and barren intrusions in the Urumieh–Dokhtar magmatic arc, Iran, constrains on geochronology and geochemistry. Ore Geol. Rev. 132, 103997.
Raeisi, D., Babazadeh, S., Long, L.E., Zhao, M., Cottle, J.M., Nayebi, N., Modabberi, S., 2024. Geochemical and isotopic signatures, and zircon U–Pb ages of the oldest known intrusive rocks associated with porphyry Cu deposits in the central Urumieh–Dokhtar magmatic arc, Iran. J. Geochem. Explor. 256, 107366.
Richards, J.P., 2022. Porphyry copper deposit formation in arcs: what are the odds? Geosphere 18 (1), 130–153.
Rostami-Hossouri, M., Ghasemi, H., Pang, K.-N., Shellnutt, J.G., Rezaei-Kahkhaei, M., Miao, L., Mobasheri, M., Iizuka, Y., Lee, H.-Y., Lin, T.-H., 2020. Geochemistry of continental alkali basalts in the Sabzevar region, northern Iran: implications for the role of pyroxenite in magma genesis. Contrib. Mineral. Petrol. 175 (1), 24.
Seedorff, E., Einaudi, M.T., Barton, M.D., Titley, S.R., 2005. Porphyry copper deposits of the southwestern United States. In: Hedenquist, J.W., Thompson, J.F.H., Goldfarb, R. J., Richards, J.P. (Eds.), Porphyry Deposits of the Americas: Their Geology, Technology, and Exploration. Society of Economic Geologists, pp. 99–123.
Shahar, A., Ziegler, K., Sossi, P.A., 2008. Iron isotopic fractionation during magmatic processes: the effects of temperature, fO_2, and the crystallization of Fe^{2+}-rich minerals. Geochim. Cosmochim. Acta 72 (22), 5409–5423.
Simmonds, V., 2019. Characteristics and timing of the Cu–Mo mineralization in the Kighal porphyry stock, NW Iran: implications for the timing of porphyry Cu-related magmatism in Iran and southern Armenia. Ore Geol. Rev. 113, 103108.
Sossi, P.A., Foden, J.D., Halverson, G.P., 2012. Redox-controlled iron isotope fractionation during magmatic differentiation: an example from the Red Hill intrusion, S. Tasmania. Contrib. Mineral. Petrol. 164 (5), 757–772.
Sossi, P.A., O'Neill, H.S.C., Eggins, S.M., 2016. The redox geochemistry of iron isotopes during partial melting of spinel lherzolite. Geochim. Cosmochim. Acta 192, 1–28.
Stracke, A., Hofmann, A.W., Hart, S.R., 2005. FOZO, HIMU, and the rest of the mantle zoo. Geochem. Geophys. Geosyst. 6, Q05007.
Tadevosyan, V., Arakelian, M., Meliksetian, K., Hovsepyan, R., 2018. Cenozoic porphyry copper and epithermal systems in Armenia: implications for mineralization in the South Armenian Block. J. Geochem. Explor. 188, 94–110.
Tang, M., Lee, C.T.A., Costin, G., Hofer, H.E., 2019. Recycling reduced iron at the base of magmatic orogens. Earth Planet. Sci. Lett. 528, 115827.
Telus, M., Dauphas, N., Moynier, F., Tissot, F.L.H., Teng, F.-Z., Nabelek, P.I., Craddock, P. R., Groat, L.A., 2012. Iron, zinc, magnesium and uranium isotopic fractionation during continental crust differentiation: the tale from migmatites, granitoids, and pegmatites. Geochim. Cosmochim. Acta 97, 247–265.
Teng, F.Z., Dauphas, N., Helz, R.T., 2008. Iron isotope fractionation during magmatic differentiation in Kilauea Iki Lava Lake. Science 320, 1620–1622.
Teng, F.Z., Dauphas, N., Huang, S., Marty, B., 2013. Iron isotopic systematics of oceanic basalts. Geochim. Cosmochim. Acta 107, 12–26.
Verdel, C., Wernicke, B.P., Hassanzadeh, J., Guest, B., 2011. A Paleogene extensional arc flare-up in Iran. Tectonics 30, TC3008.
Wang, Q., Xu, J.F., Jian, P., Bao, Z.W., Zhao, Z.H., Li, C.F., Xiong, X.L., Ma, J.L., 2006. Petrogenesis of adakitic porphyries in an extensional tectonic setting, Dexing, South China: implications for the genesis of porphyry copper mineralization. J. Petrol. 47 (1), 119–144.
Wang, Z., Huang, F., Wu, Z., 2020. Iron isotope fractionation during partial melting and melt percolation in the mantle: constraints from peridotite xenoliths from eastern China. Geochim. Cosmochim. Acta 276, 1–17.
Williams, H.M., Prytulak, J., Woodhead, J.D., Kelley, K.A., Brounce, M., Plank, T., 2018. Interplay of crystal fractionation, sulfide saturation and oxygen fugacity on the iron isotope composition of arc lavas: an example from the Marianas. Geochim. Cosmochim. Acta 226, 224–243.
Yazdani, S., Castillo, P.R., Hassanzadeh, J., 2018. Crust-mantle interaction inferred from the petrology and Sr-Nd-Pb isotope geochemistry of Eocene arc lavas from the Kahrizak Mountains, north-Central Iran. Lithos 318, 299–313.
Ye, H., Wu, C., Brzozowski, M.J., Yang, T., Zha, X., Zhao, S., Gao, B., Li, W., 2020. Calibrating equilibrium Fe isotope fractionation factors between magnetite, garnet, amphibole, and biotite. Geochim. Cosmochim. Acta 271, 78–95.
Yin, M., Li, J.X., 2011. Analysis of Rock and Minerals, vol. 2. Geological Publishing House, Beijing, pp. 1–862 (in Chinese).
Zhang, W., Hu, Z., 2020. Estimation of isotopic reference values for pure materials and geological reference materials. At. Spectrosc. 41 (3), 93–102.
Zhong, S., Li, S., Feng, C., Liu, Y., Santosh, M., He, S., Qu, H., Liu, G., Seltmann, R., Lai, Z., Wang, X., Song, Y., Zhou, J., 2021. Porphyry copper and skarn fertility of the northern Qinghai-Tibet Plateau collisional granitoids. Earth Planet. Sci. Lett. 554, 116662.